

X-ray Emission From Accretion Disks of AGN: Signatures of Supermassive Black Holes

Predrag Jovanović and Luka Č. Popović
Astronomical Observatory, Volgina 7, 11160 Belgrade, Serbia

Contents

Abstract	3
1 Introduction	3
2 Active Galactic Nuclei as Hosts of Supermassive Black Holes	5
2.1 Main characteristics of AGN	6
2.2 Classification	8
2.3 Unified model	10
3 Space-Time Geometry in Vicinity of Supermassive Black Holes	11
3.1 Historical background	12
3.2 Schwarzschild metric - non-rotating black hole	14
3.3 Kerr metric - rotating black hole	15
4 Accretion Disk Around a Supermassive Black Hole	16
4.1 Accretion rate and luminosity of AGN	17
4.2 Standard model and spectral distribution	18
4.3 Structure and emission	22
5 Supermassive Black Holes and X-ray Emission	25
5.1 X-ray continuum of AGN	26
5.2 Fe $K\alpha$ spectral line	27
5.3 Modeling of X-ray emission using ray-tracing in Kerr metric	30

5.4	Observational effects of strong gravity in the vicinity of super-massive black holes	33
6	Variability of X-ray Emission Around a Supermassive Black Hole	38
6.1	Perturbations of disk emissivity	38
6.2	Absorption by warm X-ray absorbers	42
6.3	Gravitational microlensing	45
7	Conclusion	54
	References	57

Abstract

In this chapter we discuss the X-ray radiation from relativistic accretion disks around supermassive black holes, supposed to exist in the centers of Active Galactic Nuclei (AGN). Our focus is on the X-ray radiation, especially in the Fe K α line which originates in the innermost parts of an accretion disk. Moreover, here we discuss some effects which can disturb the Fe K α profile and cause its rapid and irregular variability, observed in the X-ray spectra of some AGN. We will pay attention to three such effects: perturbations in the disk emissivity, absorption by warm absorbers and gravitational microlensing. The X-ray emission from accretion disks around non-rotating (Schwarzschild metric), as well as rotating (Kerr metric) supermassive black holes, is discussed. The X-ray radiation of AGN is probably produced in a compact region near their central supermassive black holes, and can provide us some essential information about the plasma conditions and the space-time geometry in these regions. The goal of this chapter is mainly to present a short overview of some important and recent investigations in this field.

1 Introduction

Active Galactic Nuclei are powerful sources of radiation in a wide spectral range: from γ rays to radio waves. They derive their extraordinary luminosities (sometimes more than 10,000 times higher than luminosities of "ordinary" galaxies) from energy release by matter accreting towards, and falling into, a central supermassive black hole (see e.g. Peterson, 2004).

According to the unification model of AGN (Antonucci, 1993), their central engine consists of a supermassive black hole (SMBH) with mass ranging from 10^5 to 10^9 solar masses M_{\odot} (Kaspi et al., 2000; Peterson et al., 2004), which is surrounded by an accretion disk that radiates in the X-ray band (Fabian et al., 1989). The vast majority of the X-ray sources in the Universe are AGN. The integral emission of AGN reflects the history of accretion onto SMBH over cosmic time. Emission lines are usually seen in the X-ray spectra of AGN. The broad emission Fe K α spectral line (6.4–6.9 keV, depending on ionization state) with asymmetric profile (narrow bright blue peak and a wide faint red wing) has been observed in a number of type 1 AGN (see e.g. Nandra et al., 2007). Early results from the ASCA (*Advanced Satellite for Cosmology and Astrophysics*) era suggested that broad relativistic lines

might be common in type 1 AGN. However, surprisingly, they have been detected in significant number and their features described in only a small fraction of those sources (Reynolds & Nowak, 2003). The first and the best studied one is MCG-6-30-15 (Tanaka et al., 1995; Fabian & Vaughan, 2003).

In some cases the line width corresponds to one third of speed of light, indicating that its emitters rotate with relativistic velocities. Therefore, the line is probably produced in a very compact region near the central black hole of AGN and can provide us some essential information about the plasma conditions and the space-time geometry in vicinity of the black hole. Consequently, if the line is emitted close enough to the SMBH, it shows a broad relativistic profile affected by SMBH spin (Reynolds & Fabian, 2008) and gravitational redshift (as well as other general relativistic effects) (Fabian et al., 1989; Laor, 1991).

Several studies have been performed over samples of local AGN (see e.g. Nandra et al., 1997; Yaqoob et al., 2005; Nandra et al., 2007; Bianchi et al., 2008; Markowitz et al., 2008, etc), as well as from distant quasars (Corral et al., 2008) in order to characterize the Fe $K\alpha$ emission. Nandra et al. (2007) performed a spectral analysis of a sample of 26 type 1 to 1.9 Seyferts galaxies ($z < 0.05$) observed by *XMM-Newton*. They found that a relativistic line is significantly detected in a half of their sample (54 ± 10 percent) with a mean equivalent width (EW) of ~ 80 eV, but around 30% of selected AGN showed a relativistic broad line that can be explained by the emission of an accretion disk.

Accretion disks could have different forms, dimensions, and emission, depending on the type of central black hole, whether it is rotating (Kerr metric) or non-rotating (Schwarzschild metric). They represent an efficient mechanism for extracting gravitational potential energy and converting it into radiation, giving us the most probable explanation for the main characteristics of AGN (high luminosity, compactness, jet formation, rapid time variations in radiation and the profile of the Fe $K\alpha$ spectral line).

Here we discuss the X-ray radiation from relativistic accretion disks around supermassive black holes, supposed to exist in the centers of AGN. Especially, we discuss the Fe $K\alpha$ line profile which originates from the accretion disk. Moreover, we also present some effects which can disturb the Fe $K\alpha$ profile, such as: perturbations in the disk emissivity, absorption by warm absorbers and gravitational microlensing.

The aim of this chapter is to present a short overview of results of some recent investigations in this field, and it is divided into the following six

sections: *Active Galactic Nuclei as Hosts of Supermassive Black Holes* - where the main features, classification and unified model of active galaxies are briefly presented, *Space-Time Geometry in Vicinity of Supermassive Black Holes* - where the basic definitions of Schwarzschild and Kerr metrics are given, *Accretion Disk Around a Supermassive Black Hole* - where we explain the standard model of an accretion disk, including its emission, accretion rate, luminosity, structure and spectral distribution, *Supermassive Black Holes and X-ray Emission* - where the focus is on the modeling of the observed X-ray radiation from relativistic accretion disk around a supermassive black hole of AGN in both the Fe $K\alpha$ spectral line and X-ray continuum, *Variability of X-ray Emission Around Supermassive Black Hole* - where we present the main causes of rapid and irregular variability of the X-ray emission which can be due to disk instability, reflecting in perturbations of its emissivity, or it could be caused by some external effects, such as gravitational microlensing and absorption by X-ray absorbers, and finally *Conclusion* - where the most important results from previous sections are pointed out and their brief summary is given.

Finally, we should note that a huge number of papers devoted to investigation of the X-ray emission of AGN was published in the last two decades, so it was not possible to mention all of them here, but more details and references can be found in review papers such as e.g. Brandt & Hasinger (2005); Miller (2007); Harris & Krawczynski (2006), etc.

2 Active Galactic Nuclei as Hosts of Supermassive Black Holes

Active galaxies differ from the so called "normal" galaxies in the amount of energy emitted from their nuclei. The term *Active Galactic Nuclei* (AGN) refers to the energetic phenomena in the central region of a galaxy which cannot be solely or directly produced by stars. The nebular-like emission spectra of NGC 1068, NGC 4051 and NGC 4151, with $H\alpha$, [O II] $\lambda 3727$, [Ne III] $\lambda 3869$ and [O III] $\lambda\lambda 4363, 4959, 5007$ were observed by Hubble (1926), but the first classification of these objects was made by Seyfert (1943). He recognized these objects as a class of galaxies with strong and high-excitation optical emission lines localized in the nuclei¹.

¹For more detailed historical review see Osterbrock (1989)

Active galaxies have been the subject of an intensive astrophysical investigations for the last 3 – 4 decades. As the most luminous objects with one of the most powerful energy release rates and with the most compact dimensions, AGN are of the great interest in modern astrophysics. AGN (i.e. quasars) are the brightest objects in the Universe and thus, these objects are important for the studies of the early Universe and cosmology in general. For instance, studies of their luminosity functions or quasar host galaxies are crucial for understanding the formation and evolution of galaxies in general. The class of active galaxies contains many different objects, such as quasars, gigantic elliptic radio galaxies, luminous spiral Seyfert galaxies, blazars, etc.

2.1 Main characteristics of AGN

AGN are the most luminous objects in the Universe and they have luminosities in the range from $\sim 10^{42}$ to 10^{48} erg s⁻¹, that can be 10^4 times greater than in the case of a typical galaxy. Apart from their great luminosities, AGN are emitting in the broad band of electromagnetic spectrum. The observed emission of AGN is in the continuum and in lines, from the γ and X domains to the far infrared and radio bands (see e.g. Peterson, 2004).

One of the characteristics of AGN is violent and fast variability observed in different parts of electromagnetic spectra. Fast changes in the AGN brightness are observed sometimes just for a couple of days, e.g. in the case of galaxy NGC 4151 (Shapovalova et al., 2008). This leads to the conclusion that the emission regions in the AGN have small dimensions (from only couple of light days up to couple of light months). Also, the brightness of AGN can be so high that the brightness of the host galaxy can be neglected in the total brightness (for instance in the case of quasars). Consequently, they are compact regions which could not be directly observed in the most bands of electromagnetic spectrum. Therefore, AGN and their physical/kinematical properties are indirectly studied through the analysis of their spectra.

In contrast to the spectral energy distribution (SED) of an ordinary galaxy (that represents a sum of stellar spectra, thus the most of its luminosity comes within no more than one decade of frequency), AGN emit across the broad range of frequencies (of order 10^5 Hz). The AGN continuum in a number of high-luminosity sources peaks in the ultraviolet, i.e. in the so called Big Blue Bump (BBB) (Shilds, 1978; Zhou et al., 1997). The BBB is attributed to the thermal emission from an optically thick region of the accretion disk (Shilds, 1978; Ulrich et al., 1980), or from optically thin

regions, i.e. free-free emission (Antonucci & Barvainis, 1988; Ferland et al., 1990). The observed SED in AGN is remarkably different from the thermal (black-body) spectrum of a star or a regular galaxy (Oke & Sargent, 1968). This featureless continuum observed in AGN characterizes the main source of energy input and suggests that the mechanisms that produce it are common to all types of AGN. The SED can be approximated with the power law function $F \approx \nu^\alpha$ where α is the spectral index (Krolik, 1999; Peterson, 2004).

The observed continuum of a typical Seyfert 1 galaxy is very strong compared with Seyfert 2 galaxies; as a result Seyfert 1 galaxies appear to be more luminous than Seyfert 2-s. Some AGN have the SED almost flat from the infrared to X-ray part of the spectrum, so that the spectral index is $\alpha \sim 1$, although it is usually steeper. In the radio band, the brightness of active galaxies is usually an order of magnitude higher than of normal galaxies. But still, even if it is so intensive, the radio luminosity is never higher more than 1% of the bolometric luminosity.

Another property of AGN is strong X-ray flux, with the X-ray continuum produced by lower energy photons which are Compton scattered to higher energies by relativistic electrons (Sunyaev & Titarchuk, 1980). The fraction of the power emitted in the X-ray emission is three or four times larger in AGN than in normal galaxies (Krolik, 1999; Peterson, 2004), therefore the X-emission can indicate the presence of AGN.

Today, it is widely accepted that the mechanism which powers AGN is accretion onto supermassive black hole (SMBH), i.e. the greatest part of the continuum emission comes from an accretion disk and its corona. The mass of the supermassive black hole is estimated to be from 10^5 to $10^9 M_\odot$ (Peterson et al., 2004; Peterson & Wandel, 2000). Thus, in the center of an AGN there is a supermassive black hole with an accretion disk surrounded by gas and dust in the form of a torus.

There are also other emitting regions present in the vicinity of the supermassive black hole, such as ionized gas clouds that produce intensive emission lines or jets of matter that are mostly visible in the radio band, but sometimes they can also be seen in the optical band. The kinematics of these regions is very complex as well as the physical processes that produce such specific spectra of these objects. In the central part, there are mainly three emitting line regions: Fe K α (in the X-ray range)², Broad and Narrow Line

²See §5.2 for more details

Emitting Regions (BLR and NLR, respectively; in optical/UV spectra).

In the optical and UV band, the total flux of emission (and occasionally absorption) lines contributes from several percent to tens of percent of the continuum flux. The existence of the broad and narrow emission lines comes from the fact that an AGN contains two separated emission line regions with different kinematics, density, ionization, optical thickness and radiation transfer.

The basic characteristics of the BLR and NLR can be described as follows:

- BLR is a compact region, with dimensions from only couple of light days up to couple of light weeks (Kaspi et al., 2000; Peterson et al., 2004), that is located in the vicinity of the black hole (<1 pc). The structure of this region is very complex and most likely it consists from at least two separated subregions (see e.g. Popović et al. (2004); Ilić et al. (2006); Bon et al. (2006); Popović et al. (2008), etc). The ionized gas in this region is of relatively high density ($n > 10^9 \text{cm}^{-3}$) and temperature $T \sim 10^4$ K. Emitters are moving with high velocities, up to 10000 km/s. In this region the broad emission lines (BELs) from allowed transitions are formed.
- NLR extends even up to 1 kpc far from the central source (Peterson, 2004). The density in this region is significantly smaller ($n \sim 10^3 \text{cm}^{-3}$) than in the BLR, while the temperature is on the same order of magnitude as in the BLR. From this region the narrow emission lines (NELs) arise, indicating a random motion of the emitting gas smaller than 1000 kms^{-1} . NELs are often coming from the forbidden transitions. The physical properties of this region are much closer to the properties of emission nebulae than to the BLR.

According to the different characteristics mentioned above, there are several classes of AGN.

2.2 Classification

The first group of stellar systems with active nuclei consists of Seyfert galaxies. These are spiral galaxies with very bright nuclei which spectra have strong emission lines of neutral and multi-ionized emitters. The presence of highly ionized emission lines indicates the existence of a non-stellar ionization

continuum. The presence or absence of BELs (i.e. BLR) has been historically used to separate Seyfert galaxies into two classes. Seyfert 1 galaxies have broad permitted (H I, He I and He II) and narrow permitted and forbidden lines (such as [O III] λ 5007), while Seyfert 2 galaxies have only narrow permitted and forbidden lines (Khachikian & Weedman, 1974). This simple Seyfert classification scheme can be further sub-divided according to specific spectral properties (Osterbrock, 1989), as e.g. Seyfert galaxies with intermediate Balmer profiles are classified as Seyfert 1.5-s with apparent narrow Balmer line components superimposed on broad wings.

Many low luminosity galaxies have a nucleus that resembles the Seyfert 2 nucleus, but with the spectrum that shows the forbidden lines from lower ionization states. Therefore, these galaxies are called Low-Ionization Nuclear Emission-line Regions, i.e LINERs.

Active galaxies which emit intensively in the radio band are so called radio galaxies (RG). Radio galaxies are dominantly elliptic galaxies that are divided into two morphologically different types: FR I and FR II. The classification is done according to the relative position of the surface brightness maximum (called the hot spot) in the radio lobes. For example, in the FR I radio galaxy the distance between the hot spot in the radio lobes is less than half of the maximum diameter of the radio source, while in the FR II type this distance is larger (Binney & Merrifield, 1998). Like Seyfert galaxies, radio galaxies can be divided into subgroups according to the widths of their emission lines, i.e. Narrow Line Radio Galaxies (NLRG) that emit narrow emission lines characteristic for Seyfert 2 galaxies, and Broad Line Radio Galaxies (BLRG) that emit broad lines as Seyfert 1 galaxies.

Being the most powerful sources in the Universe, quasars belong to the group of active galaxies with the absolute magnitude $M_B < -23$ (Osterbrock, 1989). These quasi stellar (quasars) objects emit intensively in the radio domain and their spectrum shows broad emission lines significantly redshifted. In this group of AGN there are also Quasi-Stellar Objects (QSOs) which have the same observed properties as quasars, except they are weak radio sources. Besides, there is a group of QSOs with broad absorption lines, so called Broad Absorption Line Quasars (BAL QSOs).

Finally, the separate class of AGN are so called BL Lacerte (Lacs) objects. BL Lacs are nuclei of elliptical galaxies that emit highly variable and polarized radiation, and have a non thermal optical continuum and a strong radio emission. With this group of galaxies, we often connect another type of AGN, Optically Violently Variable (OVVs) quasars. The OVVs, in contrast

to BL Lacs which have featureless continuum, emit broad optical emission lines characteristic for quasars. Both these groups of objects are often referred to as one class called blazars.

2.3 Unified model

As it was mentioned above, all types of AGN have some common properties. It is widely accepted that central engine of an AGN is accretion onto super-massive black hole. First observational evidence in favor of a unified model of AGN was spectropolarometric observations of Seyfert 2 galaxy NGC 1068 (Antonucci & Miller, 1985). Antonucci & Miller (1985) found broad Balmer lines and Fe II emission, characteristic of a Seyfert 1 spectrum, in the polarized spectrum of NGC 1068.

In the unified model of AGN (Antonucci, 1993) both types of Seyfert galaxies are intrinsically the same. The difference in spectral characteristics appears due to different angle of the visibility of the central regions (see Fig. 1).

A geometrically and optically thick dusty molecular torus-like structure surrounds the central source, as well as the BLR (see Fig. 1). Therefore the visibility of the nuclear engine depends on viewing angle with respect to the torus. The broad-line polarization in Seyfert 2-s is probably due to electron scattering. This picture is consistent with the differences observed between continuum fluxes of the Seyfert 1 and Seyfert 2 galaxies (Clavel et al., 2000).

Following the unified model, the line-of-sights to Seyfert 2 galaxies (or Narrow Line Objects) are obstructed by optically thick material corresponding to hydrogen column densities of $N_H > 10^{22} \text{ cm}^{-2}$ (Risaliti et al., 1999). For column densities $N_H < 10^{24} \text{ cm}^{-2}$, photons above a few keV can penetrate the torus creating an un-obstructed view of the nuclear source. In this case the source is called *Compton thin*. For column densities $10^{25} > N_H > 10^{24} \text{ cm}^{-2}$, only high energy X-ray emission (tens of keV) can pass through the obscuring material (Turner et al., 1997). But in the case $N_H > 10^{25} \text{ cm}^{-2}$ even high energy X-rays, above a few tens of keV, are Compton scattered and the nuclear source is completely hidden from our direct view. Therefore, by observing near the edge-on torus, one can detect narrow line objects, with weak (or without) X-ray emission; while by observing near the face-on torus, one can detect Blazars or OVV's. The broad line objects can be detected if one observes an inclined torus.

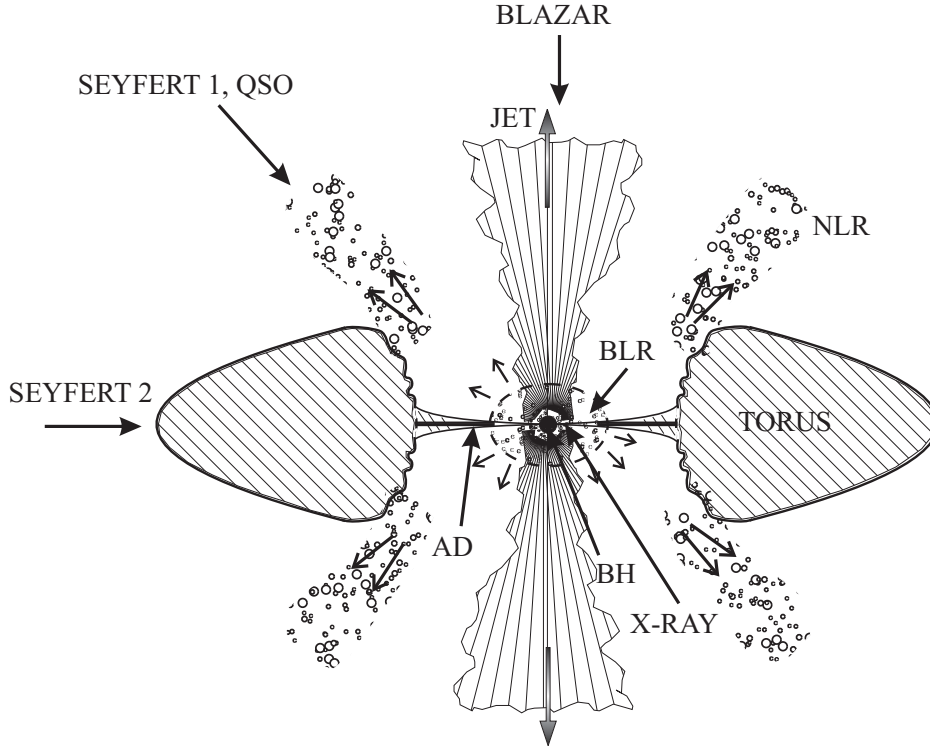


Figure 1: The scheme of unified model of AGN (Figure courtesy: Vesna Borka Jovanović).

3 Space-Time Geometry in Vicinity of Supermassive Black Holes

As it was shown in the previous section, according to unified model of AGN, in their heart there is a supermassive black hole with mass up to $10^9 M_{\odot}$, surrounded by an accretion disk. A black hole is a region of space-time around some collapsed mass which gravitational field became so powerful that nothing (including electromagnetic radiation) could escape from its attraction, after crossing the certain boundary called the event horizon (Hawking, 1988).

All black holes in nature are commonly classified according to their mass as: supermassive black holes (with masses $M_{BH} \sim 10^5 - 10^9 M_{\odot}$), intermediate-mass black holes ($M_{BH} \sim 10^2 - 10^5 M_{\odot}$), stellar-mass black holes ($M_{BH} < 10^2 M_{\odot}$), mini and micro black holes ($M_{BH} \ll M_{\odot}$). In this chapter our focus

will be on supermassive black holes located in the centers of AGN, because they are surrounded by accretion disks which X-ray radiation is the main subject of this discussion. Space-time geometry in vicinity of a supermassive black hole depends on its type (more precisely, on its angular momentum), being either non-rotating, where the local space-time geometry is described by Schwarzschild metric, or rotating, where the Kerr metric determines the geometry of local space-time.

3.1 Historical background

The term black hole was introduced in 1969 by the American scientist John Wheeler, but the predecessor of the modern idea of black holes emerged in the late eighteenth century. It was independently developed by the British geologist John Michell in 1783 and the French mathematician and astronomer Pierre-Simon Laplace in 1796. This idea was based on Newton's theory of gravity and particle theory of light, and is commonly referred to as a dark star. A dark star is, according to Michell, a sufficiently massive and compact star which have such a strong gravitational field that the corresponding surface escape velocity equals or exceeds the speed of light. Therefore, any light emitted from the surface of such star would be dragged back by the gravitational field and we would not be able to see it, but we could still feel its gravitational attraction (Hawking, 1988). After the wave theory of light was founded, the idea about a dark star was forgotten since, according to the wave theory, it was not clear that light could be affected by gravity at all.

Modern theory of black holes was founded in the twentieth century, more precisely in 1915, shortly after Einstein introduced the theory of general relativity, when the German physicist and astronomer Karl Schwarzschild found a particular exact solution to the Einstein field equations, for the limited case of a single spherical non-rotating mass.

The implications of the general relativity to the stellar evolution were firstly understood by Subrahmanyan Chandrasekhar in 1928 (Hawking, 1988). He calculated a maximum limit for the mass of a star, above which the star would not be able to support itself (by repulsion of electron degeneracy pressure which arises from Pauli exclusion principle) against its own gravity, after it had used up all its fuel. This limit ($\approx 1.5 M_{\odot}$) is nowadays known as the Chandrasekhar limit. If a star's mass is less than this limit, it can eventually stop contracting at a final state known as a "white dwarf" (Hawking, 1988). A similar discovery was made in 1932 by the Russian scientist Lev Davi-

dovich Landau. He found that there is another limiting mass ($\approx 1 - 2 M_{\odot}$), for which the corresponding final state is much smaller than a white dwarf and which would be supported against its gravity by the exclusion principle repulsion between neutrons and protons, rather than between electrons. Such stars are therefore called neutron stars (Hawking, 1988). All these results led to a surprising conclusion that a star which mass is above the Chandrasekhar limit, when it comes to the end of its fuel, could experience a catastrophic gravitational collapse to a point with an infinite density. American scientist Robert Oppenheimer was the first who explained in 1939 that, according to general relativity, stars above $\approx 3 M_{\odot}$ would at the end of their lives collapse into black holes, due to reasons given by Chandrasekhar (Hawking, 1988).

With the discovery of QSOs in the early 60s, the speculations about how their enormous luminosities could be produced within such a small region occurred. Thermonuclear reactions were not enough efficient, and therefore, they were quickly eliminated. Hoyle and Fowler suggested in 1963 that such luminosities could be produced during the collapses and disintegrations of stellar-type objects with masses of $10^5 - 10^8 M_{\odot}$ (Ferrarese & Ford, 2005). Soon, it became clear that the energy source was gravitational. For example, Wheeler suggested a mechanism in which gravitational singularity at the center of a galaxy converted the falling matter into energy (Ferrarese & Ford, 2005). Zel'dovich, Novikov and Salpeter proposed in 1964 the release of energy through accretion due the growth of a massive object at the center of a galaxy, while Lynden-Bell in 1969 made an attempt to explain the phenomena observed in QSOs and Seyfert galaxies in terms of a black hole formalism (Ferrarese & Ford, 2005). A crucial event for the acceptance of black holes was the discovery of pulsars by Jocelyn Bell in 1967, because it was the clear evidence of the existence of neutron stars, and therefore, confirmation of Chandrasekhar limit. The first detection of a solar mass black hole came in 1972, when the mass of the rapidly variable X-ray source Cygnus X-1 was proven to be above the maximum allowed for a neutron star (Ferrarese & Ford, 2005). The first convincing evidence for the existence of supermassive black holes is the discovery of the Fe $K\alpha$ spectral line in X-ray spectrum of Seyfert galaxy MGC-6-30-15 by Tanaka et al. (1995).³

Nowadays, the black hole theory is very well established, mainly due to the contributions of numerous authors during the second half of the twentieth century, like Roy Kerr, Werner Israel, John Wheeler, Brandon Carter, Roger

³See §5.2 for more details

Penrose, Stephen Hawking and many others.⁴

3.2 Schwarzschild metric - non-rotating black hole

Schwarzschild metric describes the space-time geometry in spherically symmetric gravitational field around a time-steady non-rotating black hole in vacuum. The solution of the Einstein field equations under these conditions was found by Karl Schwarzschild in 1916 (Schwarzschild, 1916a,b). If we denote the Schwarzschild radius which corresponds to a mass M by $R_S = \frac{2GM}{c^2} \approx 3 \frac{M}{M_\odot} \text{km}$ (where G is the gravitational constant and c is the speed of light), then the squared element of space-time interval ds^2 in the case of Schwarzschild metric is given by:

$$ds^2 = \left(\frac{1}{1 - \frac{R_S}{r}} \right) dr^2 - \left(1 - \frac{R_S}{r} \right) c^2 dt^2 + r^2 (d\theta^2 + \sin^2 \theta d\phi^2), \quad (1)$$

where t is the time coordinate measured by a stationary clock at infinity (which must be distinguished from the proper time τ , measured by a clock moving with the particle), r is the radial coordinate, θ is the colatitude (angle from North) in radians and ϕ is the longitude in radians.

It is obvious from Eq. (1) that Schwarzschild metric depends only on the mass M through the Schwarzschild radius R_S . The Schwarzschild metric has an infinite space-time curvature (i.e. a singularity) at $r = 0$. In the case when $r \rightarrow \infty$ this metric is reduced to the Minkowski metric of flat space-time: $ds^2 = dr^2 - c^2 dt^2 + r^2 (d\theta^2 + \sin^2 \theta d\phi^2)$.

If the complete mass M collapses below its Schwarzschild radius R_S , then it will form a spherically symmetric Schwarzschild black hole. A Schwarzschild black hole has no charge or angular momentum and it can be distinguished from any other Schwarzschild black hole only by its mass.

To a first approximation, the matter surrounding a black hole may be assumed to rotate in circular Keplerian orbits with velocity (e.g. Shakura & Sunyaev, 1973): $v^2 = \frac{GM}{R}$. Therefore, taking into account that a maximum allowed rotation velocity is speed of light ($v = c$), one can obtain so called gravita-

⁴For more detailed historical overview on this topic, see e.g. Hawking (1988)

tional radius R_g :

$$R_g = \frac{GM}{c^2} = \frac{R_S}{2} \approx 1.5 \frac{M}{M_\odot} \text{km}, \quad (2)$$

which is usually used as a unit for distance around a black hole.

3.3 Kerr metric - rotating black hole

Roy Kerr, a New Zealand mathematician, found an exact solution of the Einstein field equations of general relativity in the case of gravitational field outside an uncharged rotating black hole. The properties of Kerr solution, known as Kerr metric, are given in numerous papers and books (see e.g. Chandrasekhar, 1983; Carter, 1973) and therefore, here we will present only its definition and some basic features, necessary for the further discussion.

Contrary to the Schwarzschild case, the Kerr metric is no longer spherically symmetric. In the case of a rotating black hole with mass M and angular momentum $J = aM$, this metric is given by (see e.g. Fanton et al., 1997):

$$ds^2 = - \left(1 - \frac{2Mr}{\Sigma} \right) dt^2 - \frac{4Mar}{\Sigma} \sin^2 \theta dt d\phi + \frac{A}{\Sigma} \sin^2 \theta d\phi^2 + \frac{\Sigma}{\Delta} dr^2 + \Sigma d\theta^2, \quad (3)$$

where

$$\Sigma = r^2 + a^2 \cos^2 \theta, \quad \Delta = r^2 + a^2 - 2Mr, \quad A = (r^2 + a^2)^2 - a^2 \Delta \sin^2 \theta. \quad (4)$$

Above definition is given in Boyer-Lindquist coordinates for $c = G = 1$. As it can be seen from expressions (3) and (4), in addition to black hole mass M , the Kerr metric also depends on its specific angular momentum a . Here $a \leq M$ because any additional angular momentum would increase the energy of the black hole and, therefore, its mass (Krolik, 1999). In the case of a non-rotating black hole, i.e. for $a \rightarrow 0$, it reduces to the Schwarzschild metric.

By solving the equation $\Delta = 0$ and taking only a root with + sign, we obtain the radius of event horizon of a black hole: $r_h = M + \sqrt{M^2 - a^2}$. Thus, when $a \rightarrow 0$ then $r_h \rightarrow 2M = R_S$ (because we assumed that $c = G = 1$), whereas when $a \rightarrow M$ (i.e. for a maximally rotating black hole) then $r_h \rightarrow M$.

The minimum allowed radius r_{ms} of a stable circular equatorial orbit, or so called marginally stable orbit, is given by the roots of the equation

(Fanton et al., 1997): $r^2 - 6Mr \mp 8a\sqrt{Mr} - 3a^2 = 0$, where the upper sign refers to co-rotating orbits, while the lower one to counter-rotating orbits. In the case of Schwarzschild metric ($a = 0$) $r_{ms} = 6M$, whereas for a maximally rotating black hole ($a = M$) $r_{ms} = M$ (Fanton et al., 1997).

Rotating black holes are surrounded by a region called the ergosphere, in which there can be no static observers and the negative energy orbits are possible (Krolik, 1999). Also, there is a general relativistic effect known as frame-dragging, according to which a rotating black hole drags the space-time around itself, but such effects will not be discussed here in more details.

4 Accretion Disk Around a Supermassive Black Hole

Some observed quasars have luminosities of up to $L_{bol} \sim 10^{47}$ erg/s (Schneider, 2006). The corresponding total energy emitted during the lifetime of such quasars can be estimated to $E \geq 3 \times 10^{61}$ erg, assuming that their minimum age is about 10^7 years and that their luminosities do not change significantly over the lifetime (Schneider, 2006). Only two known mechanisms could produce such enormous amount of energy: nuclear fusion and accretion. The maximum efficiency ϵ (defined as the mass fraction of fuel that is converted into energy, according to $E = \epsilon mc^2$) of thermonuclear reactions is $\epsilon \leq 0.8\%$. Schneider (2006) showed that this value is too low to explain such high energies of $E \geq 3 \times 10^{61}$ erg. Accretion is the only remaining mechanism which can yield larger ϵ . Its maximum efficiency is about $\epsilon \sim 6\%$ for a non-rotating black hole and $\epsilon \sim 29\%$ for a maximally rotating one (Schneider, 2006). Therefore, AGN release their enormous energy by matter accreting towards, and falling into, a central supermassive black hole.

If the cold matter, which was initially at rest and without magnetic field, was subjected to free radial infall it would accrete to the central black hole without any energy release or observational effects (Shakura & Sunyaev, 1973). However, in the case of AGN the accreting matter has a significant angular momentum which does not allow its free infall. At the marginally stable orbit of central black hole with mass of $10^8 M_\odot$, the specific angular momentum is $\approx 1 \times 10^{24}$ cm²/s, which is much less even in comparison to a typical galaxy where the specific angular momentum of orbiting material is $\approx 6 \times 10^{28}$ cm²/s (Krolik, 1999). It means that approach of accreting mate-

rial toward a black hole requires a loss of the greatest fraction of its initial angular momentum. Mechanisms which can contribute to such loss of angular momentum are viscosity, nonaxisymmetric gravitational forces, magnetic forces, etc. (Krolik, 1999).

Since the orbit of minimum energy for fixed angular momentum in any spherically symmetric potential is a circle, the infall of accreting material due to loss of its angular momentum will be in form of successively smaller and smaller concentric circles. Matter traveling along orbits inclined to each other will eventually collide in the plane of intersection, and as a result, the angular momenta of different gas streams will be mixed and equalized. Consequently, all accreting matter will orbit in a single plane and will have the same specific angular momentum at any given radius, meaning that accretion is most likely performed through an accretion disk (Krolik, 1999).

The accreting material is able to approach the marginally stable orbit of central black hole only if there is an efficient mechanism for transporting angular momentum outward. Magnetic field that exists in matter flowing into the disk, as well as its turbulent motions, enable angular momentum to be transferred outward. Hence, the accretion disk is one of the best candidates for a such mechanism, since the particles in it lose their angular momentum due to friction between its adjacent layers and spiral towards black hole, releasing their gravitational energy. Part of this energy increases the kinetic energy of rotation and the rest is turned into the thermal energy and irradiated from the disk surface (Shakura & Sunyaev, 1973).

The efficiency of angular momentum transport in the disk is characterized by viscosity parameter $\alpha \leq 1$, which can be assumed as constant in most cases, since the spectrum of disk radiation and its surface temperature do not strongly depend on it, except in the case of a supercritical accretion regime (Shakura & Sunyaev, 1973).

4.1 Accretion rate and luminosity of AGN

The total energy release and the spectrum of emitted radiation are mainly determined by the rate of matter inflow into the disk on its outer boundary, i.e. by its accretion rate which is usually denoted by \dot{M} . If the accretion converts matter to radiation with fixed radiative efficiency η (in rest-mass units), then a characteristic scale for the accretion rate is the Eddington

accretion rate (Krolik, 1999; Shakura & Sunyaev, 1973):

$$\dot{M}_E = 3 \times 10^{-8} \frac{0.06}{\eta} \frac{M}{M_\odot} \frac{M_\odot}{\text{yr}}, \quad (5)$$

for which the total release of energy in the disk $L = \eta \dot{M} c^2$ is equal to the Eddington luminosity:

$$L_E = 1.51 \times 10^{38} \frac{M}{M_\odot} \frac{\text{erg}}{\text{s}}. \quad (6)$$

Eddington luminosity defines a critical luminosity for any given mass, beyond which the radiation force overpowers gravity.

Observed AGN have luminosities from $\sim 10^{42}$ to $\sim 10^{48}$ erg/s, which means that their central black holes must have masses from 10^5 to $10^9 M_\odot$, respectively (Krolik, 1999). If we assume that accretion in AGN occurs with rate of $\dot{M} \sim 0.5 M_\odot/\text{yr}$ and with radiative efficiency $\eta \sim 0.1$, the resulting luminosity would be $\sim 3 \times 10^{45}$ erg/s, which is the middle of the observed luminosity distribution of low redshifted AGN (Krolik, 1999).

Actual accretion rates \dot{M} of matter inflow into the accretion disks of AGN could be many times less or higher than the critical value of the Eddington accretion rate. At essentially subcritical accretion rates ($\dot{M} \ll \dot{M}_E$), the maximal surface temperatures T_s are on the order of $10^5 - 10^6$ K in the inner regions of the disk, from which the most of energy is released, mainly in UV and soft X-ray bands (Shakura & Sunyaev, 1973). When the accretion rate increases, the luminosity also raises, as well as the effective radiation temperature. At accretion rates comparable to \dot{M}_E , the accretion disk becomes a powerful source of X-ray radiation with the effective radiation temperature T_r from 10^7 to 10^8 K. In a strongly supercritical regime of accretion ($\dot{M} \gg \dot{M}_E$), the luminosity becomes fixed at the Eddington critical limit L_E and the most of energy is irradiated from accretion disk in UV and optical spectral bands (Shakura & Sunyaev, 1973).

4.2 Standard model and spectral distribution

By the term "standard Newtonian model of accretion disk", here we will assume the disk model given by Shakura & Sunyaev (1973). This model was originally developed to describe the accretion disks around stellar sized black holes in the binary systems, but with certain modifications it could be also applied on accretion disks around supermassive black holes in AGN.

The standard Newtonian model of accretion disk is based on the supposition that the released gravitational energy is emitted as a multitemperature blackbody radiation, where the surface temperature profile is given by (see Shakura & Sunyaev, 1973):

$$T_s(r) = \left[\frac{3}{8\pi} \frac{GM}{\sigma r^3} \dot{M} \left(1 - \sqrt{\frac{r_{in}}{r}} \right) \right]^{1/4}, \quad (7)$$

where σ is the Stefan constant, G is the gravitation constant, M is the mass of the central black hole, \dot{M} is the accretion rate and r_{in} is the inner radius of the accretion disk. In above Equation and throughout this section we will use the dimensionless disk radius r defined as (Popović et al., 2006a):

$$r = \frac{R}{6 R_g} = \frac{1}{6} \frac{Rc^2}{GM} = \frac{M_\odot}{M} \frac{R}{9 \text{ km}}, \quad (8)$$

where R is disk radius expressed in gravitational radii R_g .

In the standard model of accretion disk, accretion occurs via an optically thick and geometrically thin disk. The effective optical depth in the disk is very high and photons are close to thermal equilibrium with electrons (Popović et al., 2006a). The spectrum of thermal radiation emitted from accretion disk surface depends on its structure and temperature (and therefore on the distance to the black hole), and can have several distributions such as (Shakura & Sunyaev, 1973):

1. Planck distribution in the outer regions of the disk, where free-free and free-bound processes, as well as absorption in the lines of heavy elements broadened by the gas pressure, give the main contribution to the shape of emitted spectrum:

$$F(x) = \frac{2\pi h}{c^2} \left(\frac{kT}{h} \right)^3 \frac{x^3}{e^x - 1}, \quad (9)$$

where $x = \frac{h\nu}{kT}$, h is Planck and k is Boltzman constant,

2. more complex spectrum which passed through the homogeneous or exponentially varying medium in intermediate regions of the disk where Thomson scattering dominates and

3. Wien distribution in the inner regions where the comptonization processes strongly affect the shape of emitted spectrum:

$$F(x) \sim x^3 e^{-x}. \quad (10)$$

The surface temperature has different radial distributions in different parts of accretion disk and results in the multicolor black body spectrum. In the inner regions of accretion disks of AGN where their X-ray radiation is generated, the radial distribution of surface temperature has the following form (Popović et al., 2006b):

$$T_s(r) = T_0 r^{-3/2} (1 - r^{-1/2})^{4/5} \text{ K}, \quad (11)$$

where the temperature constant T_0 is chosen so that the corresponding effective radiation temperature is $T_r = 10^7 - 10^8$ K. This modification of standard disk model is made, because the surface temperature given by Eq. (7) could not be successfully applied in the case of accretion disks of AGN. The distribution of the temperature as a function of the accretion disk radius, according to Eq. (11), is presented in Fig. 2 for two different values of angular momentum a of central black hole (Popović et al., 2006a).

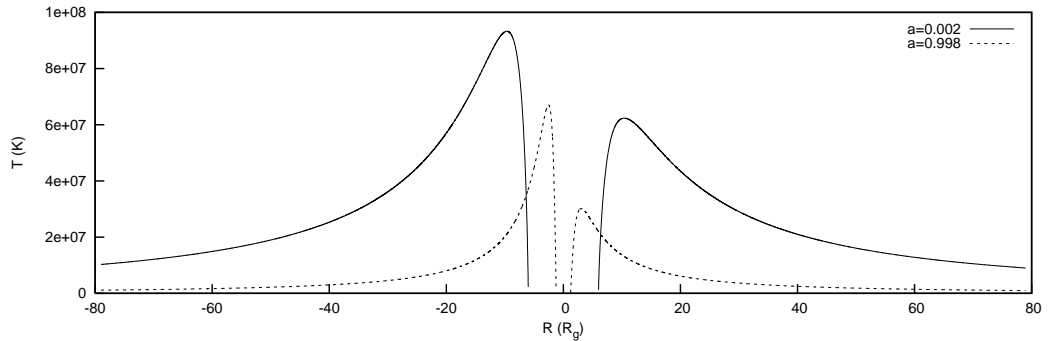


Figure 2: The distribution of the temperature as a function of the disk radius R (in the direction normal to the rotation axis, as seen by distant observer), given for two different values of angular momentum a of central black hole (Popović et al., 2006a). Negative values of R correspond to the approaching and positive to the receding side of the disk.

One can see from Fig. 2 that the temperature depends not only on disk radius, but also on its other parameters, such as e.g. angular momentum a .

Emitters located at different radii in accretion disk have different temperatures and therefore make different contributions to the observed flux. Also, it is noticeable that the temperatures at smaller radii of approaching side of the disk are significantly higher than those on its receding side.

Intensity of radiation emitted from the total disk surface can be obtained by integration of all local spectra emitted from the above regions:

$$I_\nu = 4\pi \int_{r_{in}}^{r_{out}} F_\nu [T_S(r)] r dr, \quad (12)$$

where r_{in} and r_{out} are inner and outer radii of accretion disk, respectively.

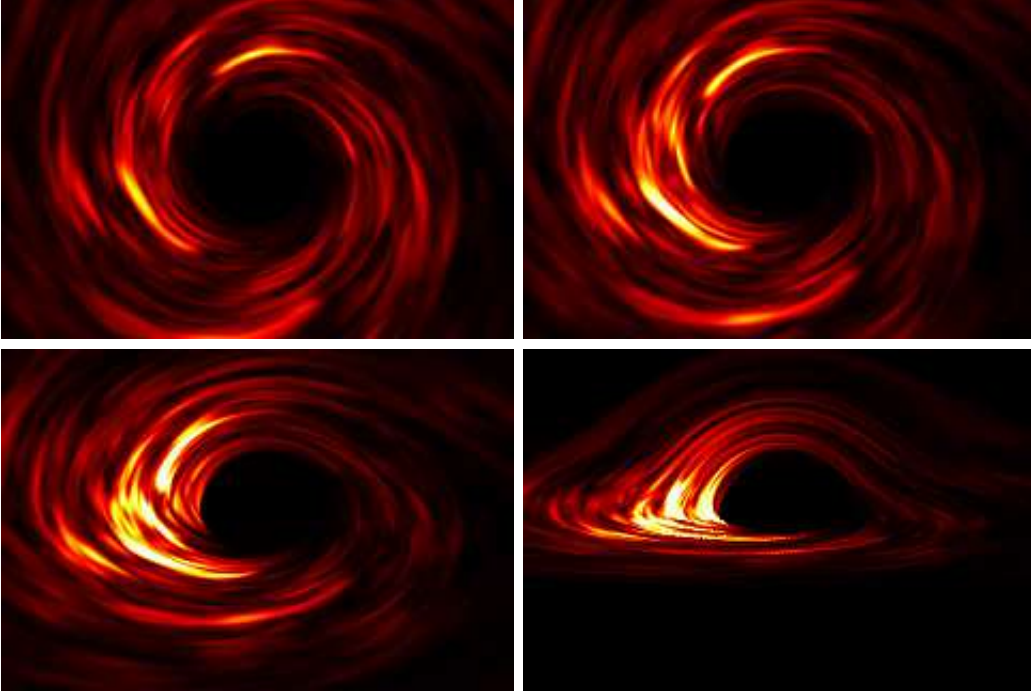


Figure 3: Magnetohydrodynamic simulations of an accretion disk as seen by a distant observer at the following inclination angles (Armitage and Reynolds, 2003): 5° (upper left), 30° (upper right), 55° (lower left) and 80° (lower right). The disk rotation is in counterclockwise direction.

Magnetohydrodynamic simulations of an accretion disk as seen by a distant observer at four different inclinations are presented in Fig. 3 (Armitage and Reynolds,

2003). The most distinctive details in this figure are especially bright regions in form of arcs within the turbulent flow, which trace out the photon trajectories close to the radius of marginally stable orbit. These arcs are much brighter on approaching side of the disk due to higher surface temperature, as shown in Fig. 2, and also due to Doppler boosting and relativistic beaming which both enhance the flux observed in the direction of motion and diminish the flux in the opposite direction.⁵

4.3 Structure and emission

An accretion disk around a supermassive black holes in the center of AGN extends from the radius of marginally stable orbit R_{ms} to the several thousands of gravitational radii. According to its radiation emitted in different spectral bands, it can be stratified in several parts (Jovanović et al., 2008):

1. innermost part close to the central black hole which emits X-rays and which extends from the radius of marginally stable orbit R_{ms} to the several tens of gravitational radii (see e.g. Ballantyne & Fabian, 2005),
2. central part ranging from $\sim 100 R_g$ to $\sim 1000 R_g$ which emits UV radiation and
3. outer part extending from several hundreds to several thousands R_g , from which the optical emission is coming (Eracleous & Halpern, 1994, 2003).

Emissivity of the disk has an important role in the line and continuum shapes. In the rest frame of the emitting material (i.e. in disk frame), emissivity $\varepsilon(r)$ is defined as energy emitted per unit proper time per unit proper area (Dabrowski et al., 1997). In the same frame, it is related to the emitted intensity $I(r, \nu_e)$ and emitted flux $F(r, \nu_e)$ by (Dabrowski et al., 1997):

$$F(r, \nu_e) = \pi I(r, \nu_e) = \varepsilon(r) \delta(\nu_e - \nu_0), \quad (13)$$

under assumption that the line emitted at frequency ν_0 can be approximated by a δ function.

Although the standard model of the accretion disk does not predict the power-law for the disk emissivity, such law is usually accepted in the case

⁵More details about the last two relativistic effects can be found in e.g. Krolik (1999)

of the hard X-ray emission from the inner parts of AGN accretion disks (Fabian et al., 1989; Nandra et al., 1997, 1999). In that case the surface emissivity is assumed to vary with radius as power law with emissivity index p (Fabian et al., 1989; Fanton et al., 1997):

$$\varepsilon(r) = \frac{\varepsilon_0}{4\pi} r^{-p}, \quad (14)$$

where ε_0 is the emissivity constant. Fabian et al. (1989) found that emissivity index p varies between 0 and 3 for the Fe K α line emitting region of Cygnus X-1, where the most probable value is $p \approx 2$. Some authors found that models describing the disk emissivity as a broken power law, rather than a single power law, achieve significantly better statistical fits of the X-ray emission in the Fe K α line (Brenneman & Reynolds, 2006). One such broken power law between some inner radius r_{in} and outer radius r_{out} with break radius r_{br} is given by (Brenneman & Reynolds, 2006):

$$\varepsilon(r) = \begin{cases} 0, & r < r_{in} \\ (r/r_{br})^{-\alpha_1}, & r_{in} \leq r < r_{br} \\ (r/r_{br})^{-\alpha_2}, & r_{br} \leq r < r_{out} \\ 0, & r \geq r_{out} \end{cases}, \quad (15)$$

where α_1 and α_2 are some emissivity indices. Using this law Brenneman & Reynolds (2006) fitted the Fe K α line of MCG–6-30-15, assuming a maximally spinning ($a = 0.998$) black hole, and found that the line emissivity followed such dependence for $\alpha_1 = 4.5 - 6$ and $\alpha_2 \sim 2.5$, where the break radius was $r_{br} \approx 6 R_g$.

The X-ray continuum can be also modeled e.g. by the following time-independent intrinsic emissivity of the disk as a function of its radius r and photon energy E (Dovčiak et al., 2004; Popović et al., 2006a):

$$I(E, r) \sim E^{-\Gamma} \times r^{-\alpha}, \quad (16)$$

where Γ is photon index and α is radial emissivity power law index of a continuum emitting region. According to some studies of observed X-ray spectra of AGN, the values of Γ and α are estimated to be about 1.5 and 2.5, respectively (Dovčiak et al., 2004; Popović et al., 2006a).

In the case of the disk outer parts (i.e. for optical emitting region), the black-body emissivity law is assumed and, according to the Eq. (9), emitted intensity is given by Planck function (Popović et al., 2006a):

$$I(E, T_s) = \frac{2E^3}{h^2 c^2} \frac{1}{e^{E/kT_s} - 1}. \quad (17)$$

However, in the inner parts of the accretion disk Planck function cannot be used properly. In these regions so called "modified" black-body emissivity law is applied. According to the Eq. (10), the corresponding emitted intensity is given by (Popović et al., 2006a):

$$I(E, T_s) \propto x^3 e^{-x}, \quad x = \frac{E}{kT_s}. \quad (18)$$

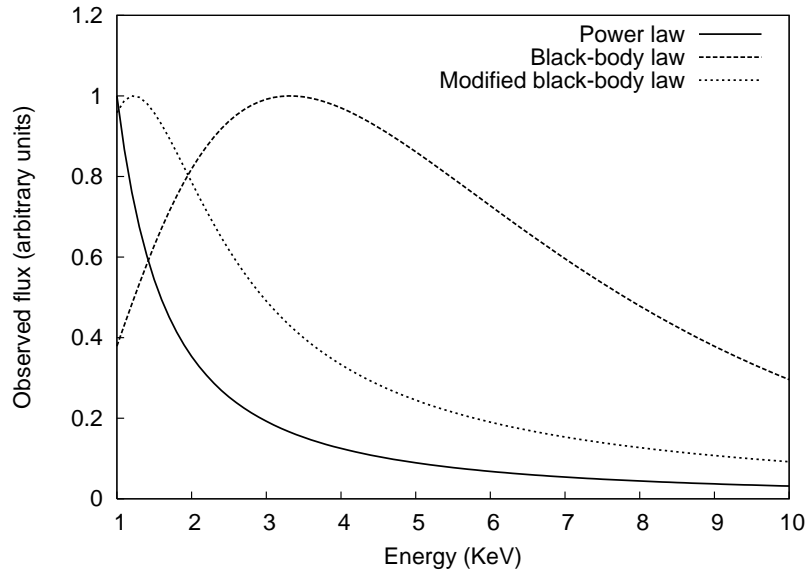


Figure 4: Shapes of the X-ray continuum in 1 – 10 keV energy band, emitted from an accretion disk with the inner and outer radii equal to $R_{in} = R_{ms}$ and $R_{out} = 80 R_g$, around a supermassive black hole with mass $M = 10^8 M_\odot$ (Popović et al., 2006a). The continuum shapes are obtained assuming the following three emissivity laws (all normalized to their maximum values): the power law defined by Eq. (14) with emissivity index $p = 2.5$, the black-body and "modified" black-body emissivity laws defined by eqs. (17) and (18), respectively, assuming the radial distribution of the surface temperature given by Eq. (11).

A comparison between the shapes of the X-ray continuum (1 – 10 keV) emitted from an accretion disk around a supermassive black hole, obtained assuming three different emissivity laws, is presented in Fig. 4 (Popović et al., 2006a). From Fig. 4 it is clear that X-ray continuum shape strongly depends on adopted emissivity law.

5 Supermassive Black Holes and X-ray Emission

A disk geometry for the X-ray emitting regions of AGN could be assumed, since the unified model of AGN includes a supermassive black hole fed by an accretion disk. Fabian et al. (1989) calculated spectral line profiles for radiation emitted from inner parts of accretion disks and later on such features of Fe $K\alpha$ lines were discovered by Tanaka et al. (1995) in Japanese *ASCA* satellite data for Seyfert galaxy MGC-6-30-15. The assumption of a disk geometry for the distribution of the X-ray emitters in the central parts of AGN is also supported by the spectral shape of the Fe $K\alpha$ line (Nandra et al., 1997, 1999, 2007). Moreover, a bump in the UV spectra of AGN is present very often, indicating that the UV and optical continua also originate from an accretion disk (Jovanović et al., 2008).

We should note here that probably most of the X-ray emission in the 1–10 keV energy range originates from inverse Compton scattering of photons from the disk by electrons in a tenuous hot corona (Jovanović et al., 2008). Proposed geometries of the hot corona of AGN include a spherical corona sandwiching the disk and a patchy corona made of a few compact regions covering a small fraction of the disk (Malzac, 2007). On the other hand, it is known that part of the accretion disk that emits in the 1–10 keV rest-frame band (e.g. the region that emits the continuum Compton reflection component and the fluorescent emission lines) is very compact and may contribute to the X-ray variability in this energy range.

A typical X-ray spectrum of AGN (see Fig. 5) is composed from the following components (Fabian, 2006):

- an underlying power-law continuum due to thermally Comptonized soft photons,
- a soft excess at low energies below 1 keV due to thermal (black-body) emission from an optically-thick accretion disk,
- a fluorescent/recombination Fe $K\alpha$ line and
- a Compton hump due to X-ray reflection from the disk.

In the following text we will discuss in more details power law component of X-ray continuum and the Fe $K\alpha$ spectral line.

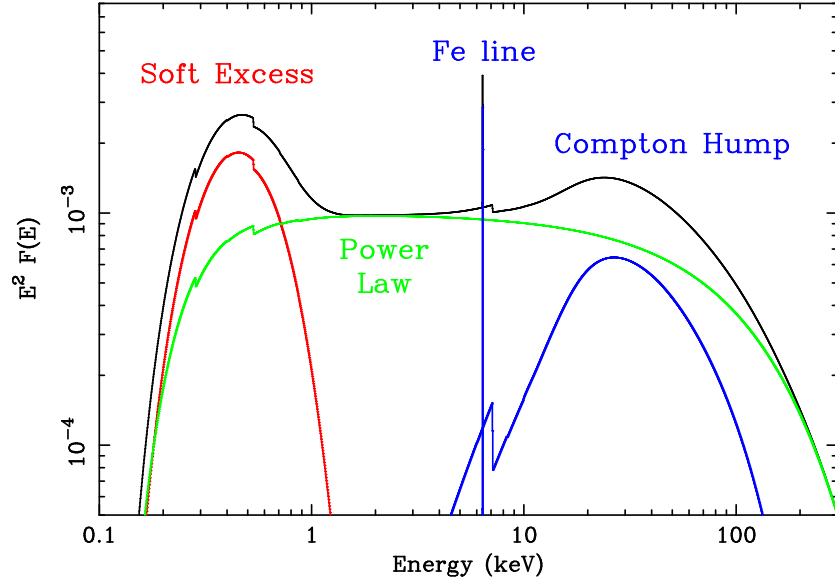


Figure 5: A typical X-ray spectrum of an AGN (Fabian, 2006).

5.1 X-ray continuum of AGN

AGN are powerful sources of X-ray radiation in the continuum from 0.1 to 100 keV, which contains two components (see Fig. 6): the soft X-rays with a steep spectrum and the hard component with spectrum in form of a power law (Fabian et al., 1989; Fabian, 2006). Therefore, the observed continuum flux is very often fitted with one or two black-body components in the soft X-rays, in addition to a power law component in the hard X-rays. It is believed that both, soft and hard components mostly arise from the inner region of AGN disk, close to the central supermassive black hole ($\sim 10 R_S$). The first component is probably formed in the accretion disk, which is also a strong source of the soft UV and optical photons, or at least in cold ($T < 10^7$ K) accreting gas clouds. The second one is caused by high-energy (most likely relativistic) electrons in hot corona above the disk, when they multiply inverse-Compton scatter some of the low-energy UV and optical photons from the disk to X-ray energies (Fabian et al., 1989, 2000). The resulting hard X-ray power law component irradiates the accretion disk and produces a reflection component which causes the observed spectrum to flatten above 10 keV (see Fig. 6), as Compton recoil reduces the backscattered flux (Fabian et al., 2000). Apart from its own thermal radiation, the cold gas around a black hole is also ir-

radiated by these hard X-ray photons, producing different spectral features through photoelectric absorption, fluorescence (responsible for occurrence of fluorescent iron lines) and scattering (Fabian et al., 1989). Therefore, the observed X-ray spectra of AGN consist of an iron line spectrum superposed on a power law continuum (Fabian et al., 2000).

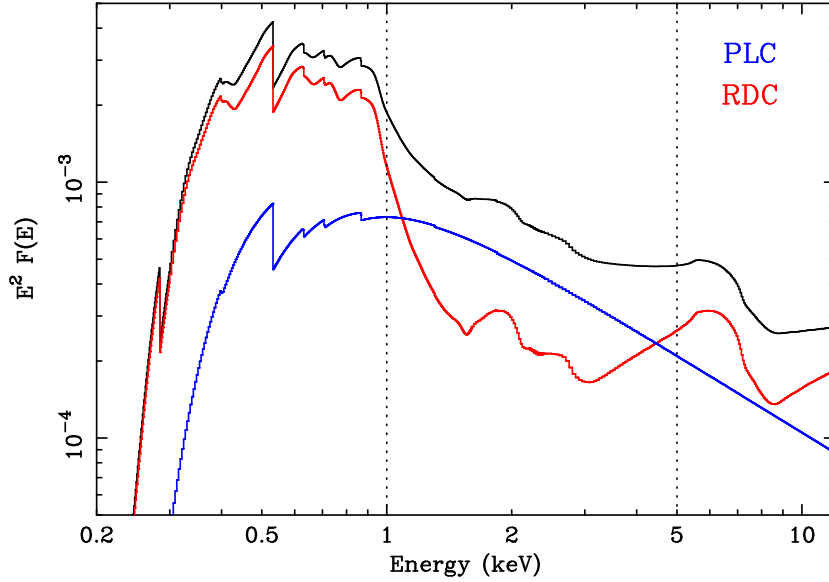


Figure 6: The two-component model of the X-ray continuum in the case of Seyfert 1 galaxy 1H 0707–495, composed from a power law (PLC) and a reflection (RDC) component (Fabian, 2006).

Fluctuations of the X-ray radiation on timescales from several parts of an hour until several days are a common property of all AGN (Krolik, 1999). Such fast variations confirm assumption that X-ray radiation is emitted from a very compact region in the center of AGN.

Fabian (2006) showed that a two-component model, consisting of a power-law and a reflection component, could better describe the observed variability of X-ray spectra in the case of several bright Seyferts than a simple power-law model. This two-component model is presented in Fig. 6.

5.2 Fe $K\alpha$ spectral line

Contrary to the UV and optical spectra of AGN, there are very few strong spectral lines in their X-ray spectra. The most important one is the Fe $K\alpha$

line. Iron abundance in accretion disks of AGN is sufficient to produce very strong emission in this line. The CCD detectors on Japanese *ASCA* satellite were the first instruments with sufficient spectral resolution and sensitivity in the X-ray band, by which Tanaka et al. (1995) obtained the first convincing proof for the existence of the Fe $K\alpha$ line in AGN spectra. This discovery was made after four-day observations of Seyfert 1 galaxy MCG-6-30-15 (see Fig. 7).

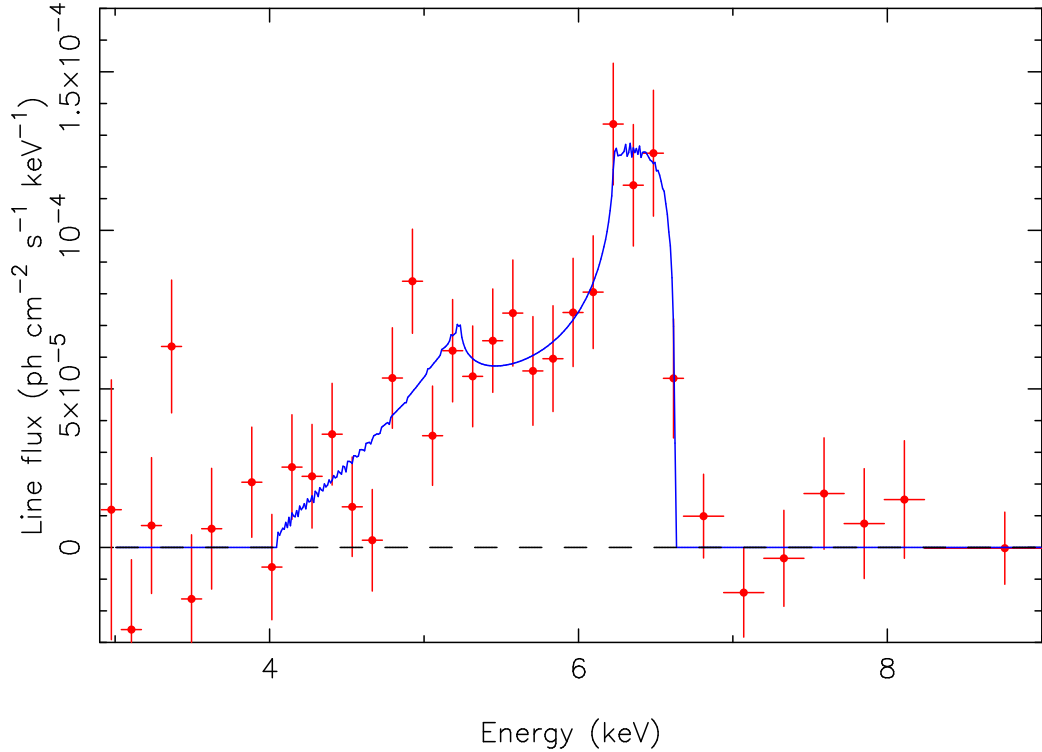


Figure 7: The profile of the Fe $K\alpha$ line from Seyfert 1 galaxy MCG-6-30-15 observed by *ASCA SIS* detector (Tanaka et al., 1995) and the best fit (blue solid line) obtained by a model of the accretion disk in Schwarzschild metric, extending between 3 and 10 Schwarzschild radii (Fabian et al., 1989). Image Credit: Tanaka et al., Copyright: Nature, 375, 659, 1995. Image generated by Dr. Paul Nandra NASA/GSFC.

The fluorescent/recombination iron $K\alpha$ line is an important indicator of accreting flows around compact objects, because it is produced in inner parts of their accretion disks. At the same time, it is the strongest line of the X-ray

radiation, and it can be found in the spectra of all types of accreting sources: binary black hole and neutron star systems, cataclysmic variable stars and AGN.

The Fe $K\alpha$ line is produced when plasma is subjected to the influence of the hard X-ray radiation so that one of the two K -shell ($n = 1$, where n is the principal quantum number) electrons of an iron atom (or ion) is ejected following the photoelectric absorption of an X-ray (Fabian et al., 2000). The threshold for the absorption by neutral iron is 7.1 keV (Fabian et al., 2000). The resulting excited state decays when an L -shell ($n = 2$) electron drops into the K -shell, releasing 6.4 keV of energy. This energy is either emitted as an emission-line photon (34% probability) or internally absorbed by another electron (66% probability) which is consequently ejected from the iron ion (Auger effect).

The fluorescent yield (i.e. the probability that photoelectric absorption is followed by fluorescent line emission rather than the Auger effect) is a weak function of the ionization state from neutral iron (Fe I) up to Fe XXIII (Fabian et al., 2000). For lithium-like iron (Fe XXIV) through to hydrogen-like iron (Fe XXVI), the lack of at least two electrons in the L -shell means that the Auger effect cannot occur. For He and H-like iron ions, the line is produced by the capture of free electrons (recombination) and the equivalent fluorescent yield is high and it depends on the plasma conditions (Fabian et al., 2000).

For the neutral iron, the Fe $K\alpha$ line energy is 6.4 keV (more precisely, there are two components of the line (Fabian et al., 2000): Fe $K\alpha_1$ at 6.404 and Fe $K\alpha_2$ at 6.391 keV), while in the case of ionization, the energy of both the photoelectric threshold and the Fe $K\alpha$ line are slightly increased. Even for such high ionization states of He and H-like iron ions, the Fe $K\alpha$ line energy is increased only to 6.7 and 6.9 keV, respectively (Krolik, 1999).

Fe $K\alpha$ line is pretty narrow in itself, but in case when it originates from a relativistically rotating accretion disk of AGN it becomes wider due to kinematical effects, and also its shape (or profile) is changed due to Doppler boosting and gravitational redshift. Such broadening of the line is very often observed in spectra of Seyfert galaxies and is one of the main evidences for the existence of a relativistic accretion disk which extends deeply in the gravitational field of the central black hole (Życki, 2004). If the line originated from an arbitrary radius of a nonrelativistic (Keplerian) accretion disk it would have a symmetrical profile (due to Doppler effect) with two peaks: a "blue" one which is produced by emitting material from the approaching

side of the disk in respect to an observer, and a "red" one which corresponds to emitting material from the receding side of the disk. The widest parts of the Fe $K\alpha$ line arise from the innermost regions of the disk, where the rotation of emitting material is the fastest. Using *ASCA* satellite observations, Nandra et al. (1997) found that, in case of 14 Seyfert 1 galaxies, Full-Widths at Half-Maximum (FWHM) of their Fe $K\alpha$ lines correspond to velocities of $\approx 50,000$ km/s. In some cases (e.g. for Seyfert 1 galaxy MCG-6-30-15), FWHM velocity reaches 30% of speed of light (see e.g. Nandra et al., 2007). It means that in the vicinity of the central black hole, orbital velocities of the emitting material are relativistic, causing the enhancement of the Fe $K\alpha$ line "blue" peak in regard to its "red" peak (relativistic beaming). Taking into account the integral emission in the line over all radii of accretion disk, one can obtain the line with asymmetrical and highly broadened profile (Fabian et al., 2000). The "blue" peak is then very narrow and bright, while the "red" one is wider and much fainter (see Fig. 7). Besides, the gravitational redshift causes further deformations of the Fe $K\alpha$ line profile by smearing the "blue" emission into "red" one. Since the observed Fe $K\alpha$ line profiles are strongly affected by such relativistic effects, they represent a fundamental tool for investigating the plasma conditions and the space-time geometry in the vicinity of the supermassive black holes of AGN.

One of the important features of the Fe $K\alpha$ line is variability of both, its shape and intensity. Observed variations of this line are surprisingly less than those of the high energetic continuum, which is assumed to give rise to the line emission (Życki, 2004). Also, it seems that there is a lack of corresponding line response to the continuum variations on time scales from several minutes to several days, or that these line and continuum variations are uncorrelated (Życki, 2004). In §6 of this chapter we will pay attention to some possible causes of such behavior of the Fe $K\alpha$ line and X-ray continuum.

5.3 Modeling of X-ray emission using ray-tracing in Kerr metric

The disk emission can be analyzed by numerical simulations, based on so called ray-tracing method in Kerr metric (Bao et al., 1994; Bromley et al., 1997; Fanton et al., 1997; Čadež et al., 1998), taking into account only photon trajectories reaching the observer's sky plane. In this method one divides the image of the disk on the observer's sky into a number of small elements

(pixels). For each pixel, the photon trajectory is traced backward from the observer by following the geodesics in a Kerr space-time, until it crosses the plane of the disk (see Fig. 8). Then, the flux density of the radiation emitted by the disk at that point, as well as the redshift factor of the photon are calculated. In that way, one can obtain the color images of the accretion disk which a distant observer would see by a high resolution telescope. The simulated line profiles can be calculated taking into account the intensities and received photon energies of all pixels of the corresponding disk image. All illustrations of the accretion disk and the line shape in this chapter are obtained using such numerical simulations. Here we will briefly describe a pseudo-analytical approach of ray-tracing proposed by Čadež et al. (1998).

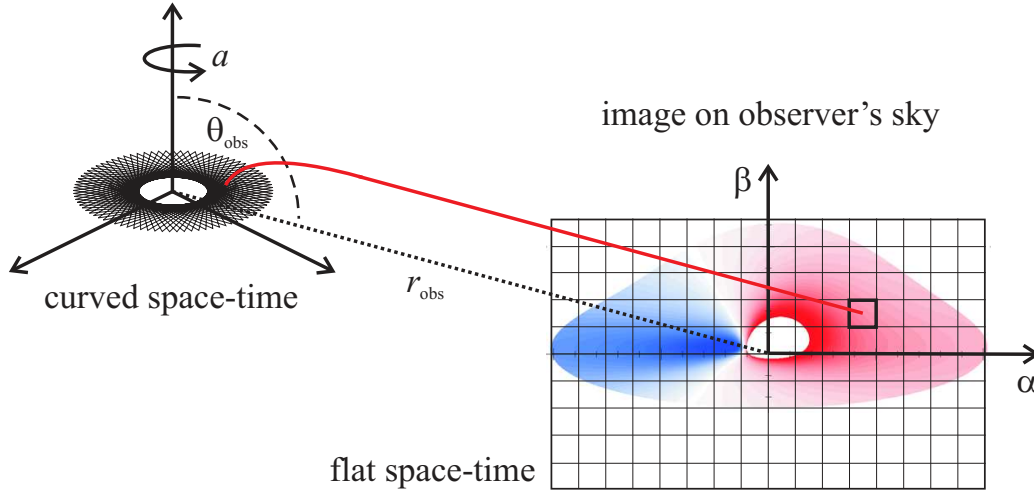


Figure 8: Schematic illustration of the ray-tracing method in the Kerr metric, showing a light ray emitted from some radius of accretion disk in coordinate system defined by a rotating black hole with angular momentum a , and observed at a pixel with coordinates (impact parameters) α, β on the disk image in the observer's reference frame (Figure courtesy: Vesna Borika Jovanović).

This method is based on the pseudo-analytical integration of the geodesic equations which describe the photon trajectories in the general case of a rotating black hole having some angular momentum J , which gravitational field is therefore described by the Kerr metric (see §3.2 for more details). The Kerr metric depends on the angular momentum normalized to the mass M of black hole: $a = J/Mc$, $0 \leq a \leq M$.

A photon trajectory in the Kerr metric can be described by three constants of motion (the energy at infinity and two constants related to the angular momentum, respectively) which have the following forms when natural units $c = G = M = 1$ are assumed (Čadež et al., 1998): $E = -p_t$, $\Lambda = p_\phi$ and $Q = p_\theta^2 - a^2 E^2 \cos^2 \theta + \Lambda^2 \cot^2 \theta$. Here, (r, θ, ϕ, t) are the usual Boyer-Lindquist coordinates and p is the 4-momentum. As the trajectory of a photon is independent on its energy, it may be expressed using the two dimensionless parameters $\lambda = \Lambda/E$ and $q = Q^{1/2}/E$ which are very simply related to the two impact parameters α and β describing the apparent position on the observer's celestial sphere: $\alpha = -\frac{\lambda}{\sin \theta_{obs}}$ and $\beta = \pm (q^2 + a^2 \cos^2 \theta_{obs} - \lambda^2 \cot^2 \theta_{obs})^{\frac{1}{2}}$,

where the sign of β is determined by $\left(\frac{dr}{d\theta}\right)_{obs}$.

In order to find the photon trajectories (null geodesics) which originate in the accretion disk at some emission radius r_{em} and reach the observer at infinity, one must solve the following integral equation (Čadež et al., 1998):

$$\pm \int_{r_{em}}^{\infty} \frac{dr}{\sqrt{R(r, \lambda, q)}} = \pm \int_{\theta_{em}}^{\theta_{obs}} \frac{d\theta}{\sqrt{\Theta(\theta, \lambda, q)}}, \quad (19)$$

$$\begin{aligned} R(r, \lambda, q) &= (r^2 + a^2 - a\lambda)^2 - \Delta[(\lambda - a)^2 + q^2], \\ \Theta(\theta, \lambda, q) &= q^2 + a^2 \cos^2 \theta - \lambda^2 \cot^2 \theta. \end{aligned} \quad (20)$$

Above integral Equation (19) can be solved in terms of Jacobian elliptic functions, and therefore it is a pseudo-analytical integration. For the exact expressions of the solutions, see e.g. Čadež et al. (1998), or more recent paper from Li et al. (2005).

Due to relativistic effects, photons emitted at frequency ν_{em} will reach infinity at frequency ν_{obs} , and their ratio determines the shift due to these effects: $g = \frac{\nu_{obs}}{\nu_{em}}$. The total observed flux at the observed energy E_{obs} is given by (Fanton et al., 1997):

$$F_{obs}(E_{obs}) = \int_{image} \varepsilon(r) g^4 \delta(E_{obs} - gE_0) d\Xi, \quad (21)$$

where $\varepsilon(r)$ is the disk emissivity, $d\Xi$ is the solid angle subtended by the disk in the observer's sky and E_0 is the rest energy.

A simulated accretion disk image is obtained in the following way:

1. values of the following input parameters are specified: inner and outer radii (R_{in} and R_{out}) of the disk, angular momentum a of the central black hole, observer's viewing angle (disk inclination) θ_{obs} (also, often denoted by i) and parameters defining the disk emissivity
2. constants of motion λ and q are calculated for each pixel on imaginary observer's photographic plate (i.e. for each pair of impact parameters α and β)
3. geodesic Equation (19) is integrated for each pair of λ and q
4. values of shift due to relativistic effects g and observed flux F_{obs} are calculated
5. pixels on imaginary observer's photographic plate are colored according to the value of shift g and a simulated disk image is obtained.

The simulated line profiles can be calculated from the corresponding disk images by binning the observed flux at all pixels over the bins of shift g . The examples of simulated disk images obtained in such way are presented in left panels of Figs. 9 - 11, and the corresponding simulated line profiles are presented in the right panels of the same figures.

5.4 Observational effects of strong gravity in the vicinity of supermassive black holes

In general, black holes have three measurable parameters (not including the Hawking temperature): charge, mass (and hence gravitational field) and angular momentum (or spin). In the case of supermassive black holes of AGN, only the latter two are of sufficient importance because they are responsible for several effects which can be detected in the observed Fe $K\alpha$ line shapes (Jovanović and Popović, 2008a).

In order to study the size of the Fe $K\alpha$ line emitting region, as well as its location in the disk, one can assume that the line is emitted from a region in form of a narrow ring. For example, Jovanović and Popović (2008a) assumed a line emitting region with width equals to $1 R_g$, located between: a) $R_{in} = 6 R_g$ and $R_{out} = 7 R_g$ and b) $R_{in} = 50 R_g$ and $R_{out} = 51 R_g$. These two cases are presented in Fig. 9.

From Fig. 9 one can see how the Fe $K\alpha$ line profile is changing as the function of distance from central black hole. When the line emitters are located at the lower radii of the disk, i.e. closer to the central black hole, they rotate faster and the line is broader and more asymmetric (see Fig. 9

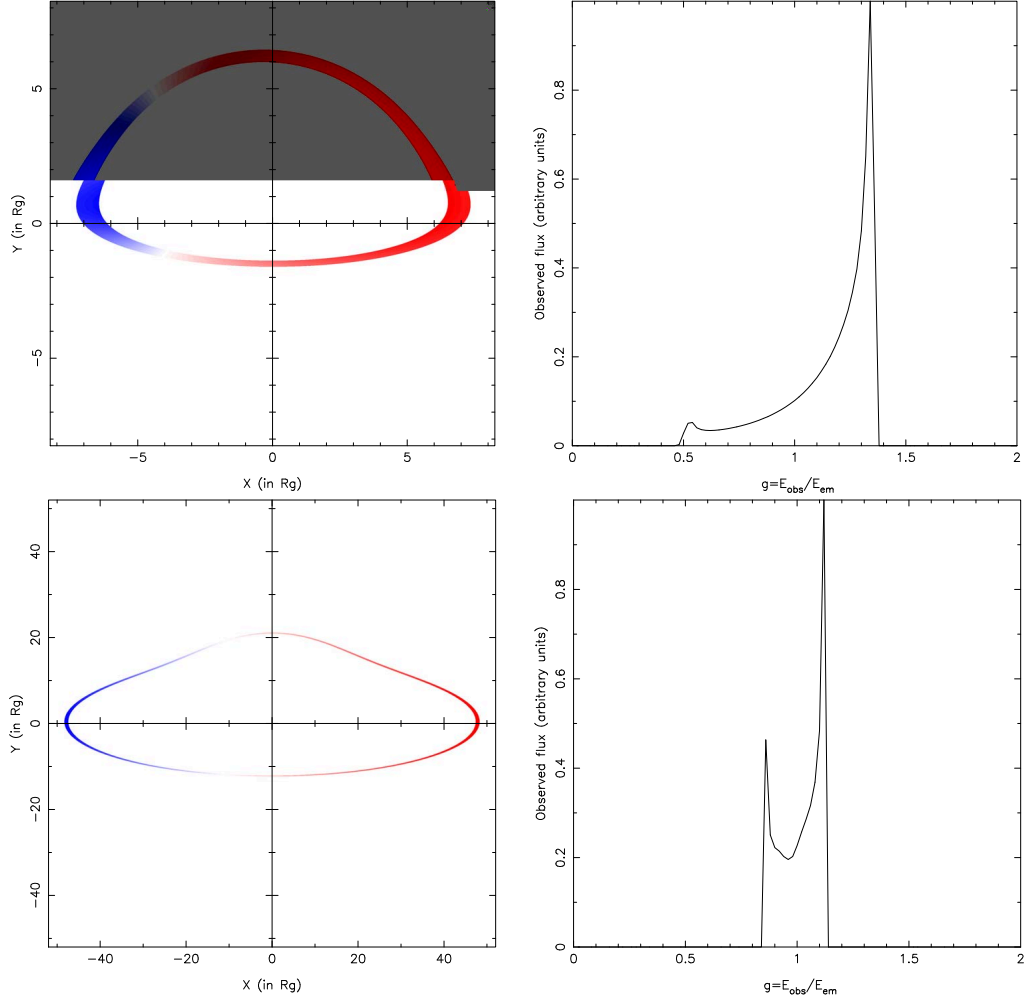


Figure 9: *Left*: illustrations of the Fe $K\alpha$ line emitting region in form of narrow ring with width = $1R_g$, extending from: $R_{in} = 6 R_g$ to $R_{out} = 7 R_g$ (top) and $R_{in} = 50 R_g$ to $R_{out} = 51 R_g$ (bottom). *Right*: the corresponding Fe $K\alpha$ line profiles (Jovanović and Popović, 2008a).

top-right). If the line emission is originating at larger distances from the black hole, its emitting material is rotating slower and therefore the line becomes narrower and more symmetric (see Fig. 9 bottom-right). In majority of AGN, where the broad Fe $K\alpha$ line is observed, its profile is more similar to the modeled profile as obtained under assumption that the line emitters are located close to the central black hole (Tanaka et al., 1995; Nandra et al.,

2007; Jovanović and Popović, 2008a).

Angular momentum or spin of the central supermassive black hole of AGN is a property of the space-time metric. To demonstrate how it affects the observed line profiles we will now assume that the Fe $K\alpha$ line emitting region extends between the following inner and outer radii: $R_{in} = R_{ms}$ and $R_{out} = 20 R_g$. We will analyze the following two cases for accretion disk inclination in both Schwarzschild and Kerr metrics: (i) $i = 35^\circ$ and (ii) $i = 75^\circ$. In the case of Schwarzschild metric we have a stationary black hole and hence, angular momentum (normalized to the mass of black hole) is $a = 0$. In Kerr metric (i.e. for a rotating black hole), it can take any value from the $[0, 1]$ range, but in these two examples we will assume an almost maximally rotating black hole with $a = 0.998$.

Illustrations of an accretion disk and the corresponding Fe $K\alpha$ line shapes in the first case are presented in Fig. 10. As one can see from Fig. 10, the red peak of the Fe $K\alpha$ line is brighter in case of almost maximally rotating black hole, but at the same time it is also more embedded into the blue peak wing and therefore less separable from it.

Fig. 11 contains illustrations of the line emitting regions and the corresponding line shapes in the case of a highly inclined disk ($i = 75^\circ$). Here, the line profiles are broader than in the first case, mostly due to higher inclination. As it can be seen from Fig. 11, in the case of the Kerr metric, the red peak of the line is again more embedded into its blue peak wing (as in the first case) and it confirms that this effect can be most likely attributed to angular momentum (Jovanović and Popović, 2008a). Consequently, angular momentum of the central black hole has significant influence on the line shape which supports assumption that the line originates from the innermost part of accretion disk, close to the central black hole (see e.g. Ballantyne & Fabian, 2005). This fact can be used for estimation of angular momentum of the central black hole in observed AGN.

Above simulations of the strong gravitational field influence on the Fe $K\alpha$ line show that such effects can be detected in the observed line shapes and therefore, comparisons between the observed and modeled Fe $K\alpha$ line profiles (see e.g. Fig. 7) can bring us some essential information about the strong gravitational field in the vicinity of central supermassive black holes of AGN (Nandra et al., 2007).

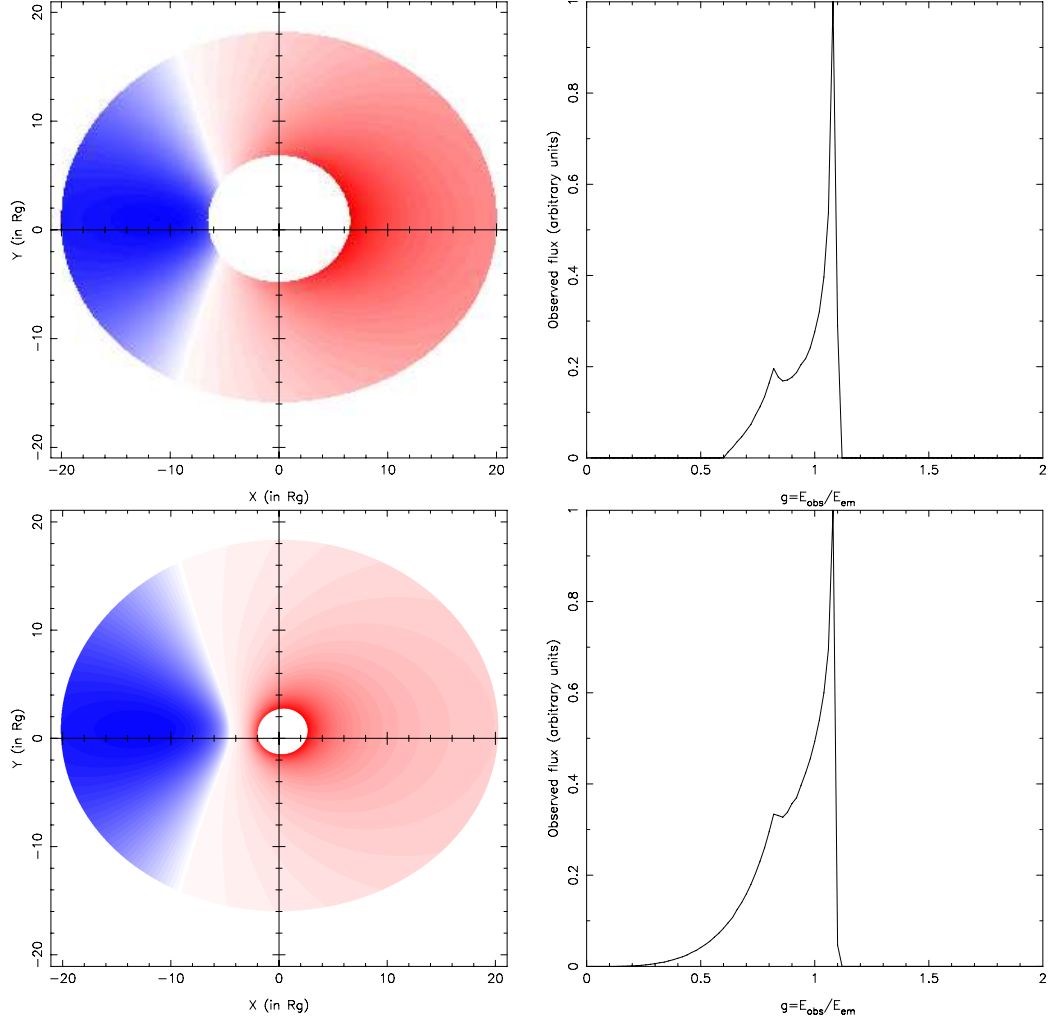


Figure 10: Illustrations of accretion disk (left) and the corresponding Fe $K\alpha$ line profiles (right) in the case of Schwarzschild (top) and Kerr metric with angular momentum $a = 0.998$ (bottom). The disk inclination is $i = 35^\circ$ and its inner and outer radii are $R_{in} = R_{ms}$ and $R_{out} = 20 R_g$, respectively (Jovanović and Popović, 2008a).

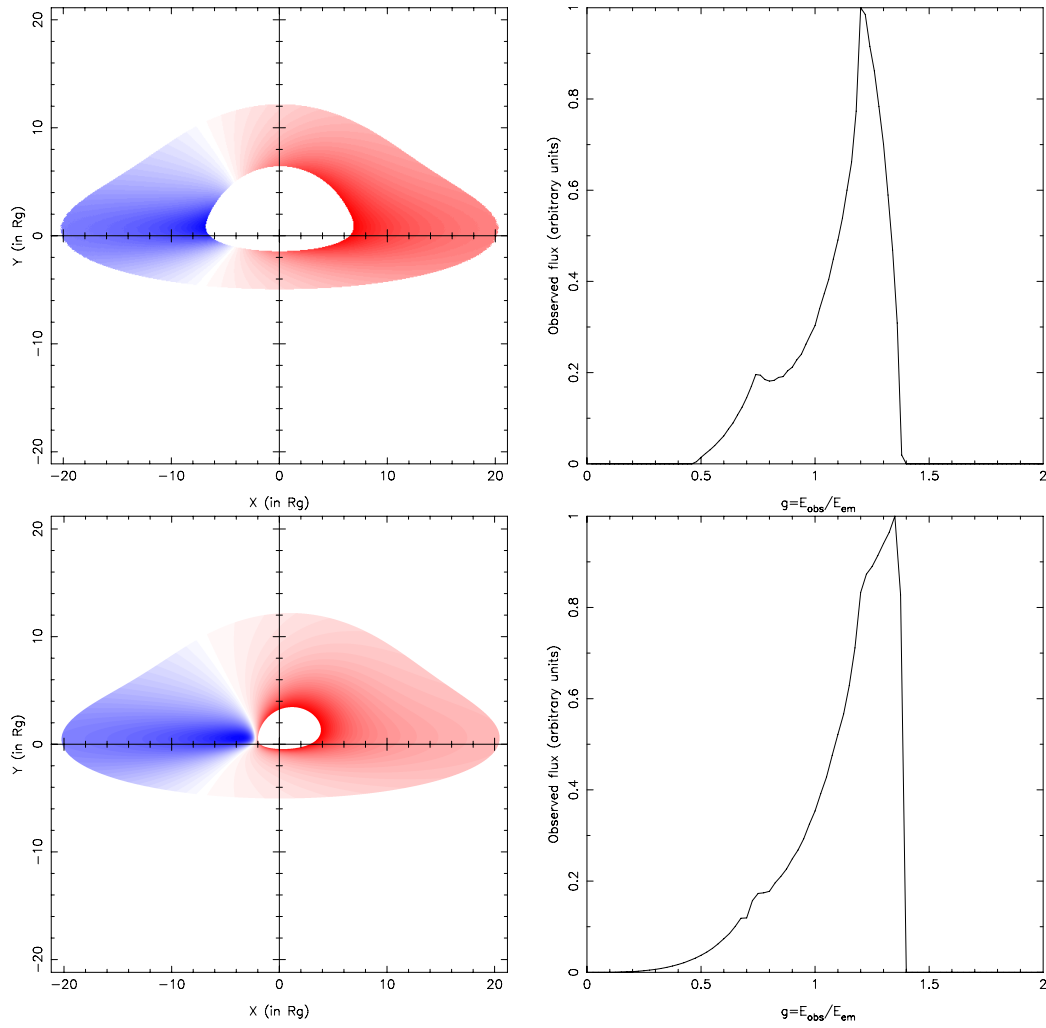


Figure 11: The same as in Fig. 10, but for a highly inclined disk with $i = 75^\circ$ (Jovanović and Popović, 2008a).

6 Variability of X-ray Emission Around a Supermassive Black Hole

Rapid and irregular variability of the observed X-ray emission in the line, as well as in the continuum, is a common property of all AGN. This variability could be due to disk instability, reflecting in perturbations of the disk emissivity, or it could be caused by some external effects, such as gravitational microlensing and absorption by X-ray absorbers. We developed a model of perturbations of the disk emissivity, a model of absorption region and three models of gravitational microlensing. In the following text we will pay more attention to all three mentioned causes of the X-ray variability in AGN.

6.1 Perturbations of disk emissivity

In some cases the observed X-ray variability of AGN cannot be explained by the standard model of accretion disk. For example, in addition to the stable 6.4 keV core of the Fe K α line, a variable "red" feature of the line at 6.1 keV is also detected in X-ray spectrum of Seyfert galaxy NGC 3516 (see Fig. 12), observed by *XMM-Newton* satellite (Iwasawa et al., 2004). This feature varies systematically in the flux at intervals of 25 ks and in energy between 5.7 and 6.5 keV. Iwasawa et al. (2004) found that the spectral evolution of the "red" feature agrees well with hypothesis of an orbiting spot in the accretion disk.

Many processes in the accretion disk may lead to perturbations in its emissivity, such as self gravity, disk-star collisions and baroclinic vorticity (Flohic & Eracleous, 2008). Different models of emissivity perturbing regions can be used to describe the observed variability in the Fe K α line profiles and intensities, like stochastically perturbed one given by Flohic & Eracleous (2008), but here we will present a bright spot model given by Jovanović and Popović (2008b). In this model a modification of the power-law disk emissivity is proposed in order to explain the observed profiles. The following emissivity law of the disk is assumed:

$$\varepsilon_1(x_p, y_p) = \varepsilon(r(x_p, y_p)) \cdot \left(1 + \varepsilon_p \cdot e^{-\left(\left(\frac{x - x_p}{w_x} \right)^2 + \left(\frac{y - y_p}{w_y} \right)^2 \right)} \right), \quad (22)$$

where $\varepsilon_1(x_p, y_p)$ is the modified disk emissivity at the given position (x_p, y_p)

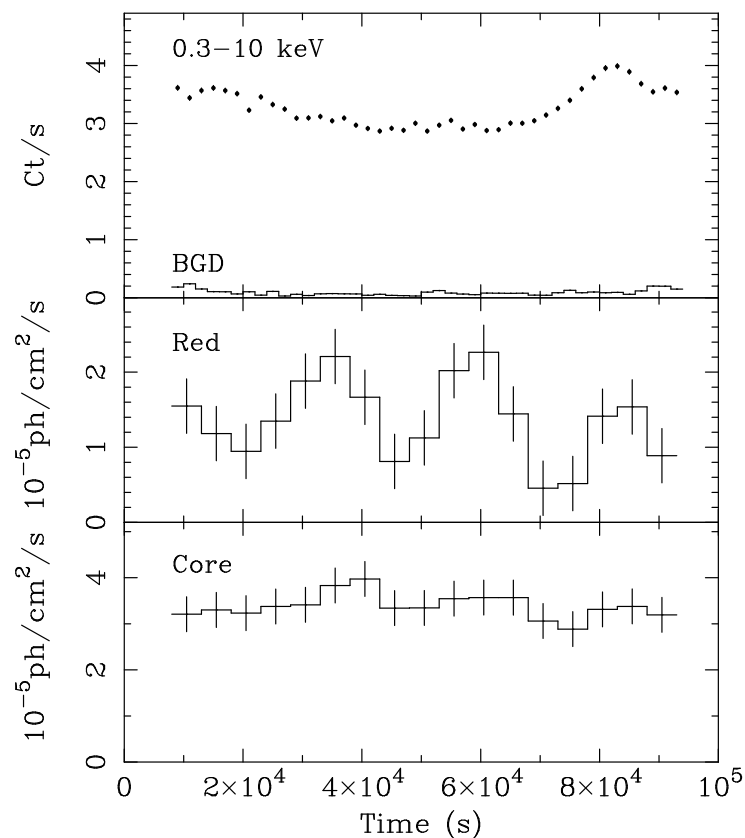


Figure 12: Light curves of Seyfert galaxy NGC 3516 (Iwasawa et al., 2004) for: the 0.3 – 10 keV band (top), the Fe $K\alpha$ line red feature (middle) and the 6.4 keV line core (bottom).

of perturbing region (in gravitational radii R_g), $\varepsilon(r(x_p, y_p))$ is the power-law disk emissivity at the same position, ε_p is emissivity of perturbing region and (w_x, w_y) are its widths (also in R_g).

An example of the shape of the perturbed emissivity for an accretion disk in Schwarzschild metric, as well as the corresponding perturbed and unperturbed Fe $K\alpha$ line profiles, are presented in the left and right panels of Fig. 13, respectively.

As one can see from Fig. 13, when perturbation moves along receding side of the disk (positive direction of x -axis), the perturbing model affects only "red" part of the line flux, while the "blue" one stays nearly constant, as well as the line core. Therefore, this bright spot model of perturbing region

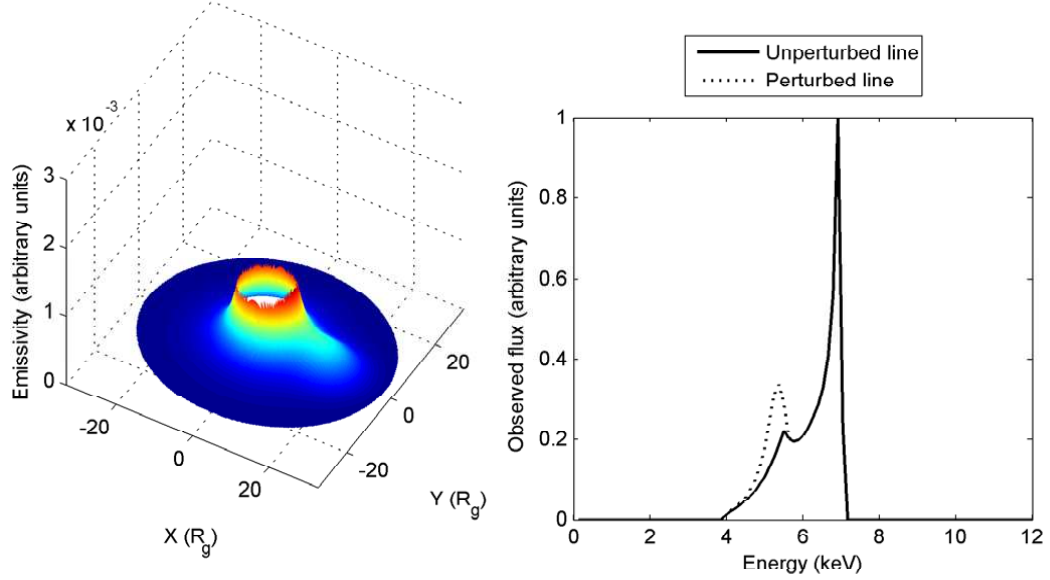


Figure 13: *Left:* shape of perturbed emissivity of an accretion disk in Schwarzschild metric for the following parameters of perturbing region: $x_p = 20 R_g$, $y_p = 0$ and $w_x = w_y = 7 R_g$ (Jovanović and Popović, 2008b). *Right:* the corresponding perturbed (dashed line) and unperturbed (solid line) Fe $K\alpha$ line profiles.

could satisfactorily explain the observed variations of the Fe $K\alpha$ line flux.

Under assumption that perturbation moves by speed of light c , one can also calculate time t_p [s] that corresponds to the current position (x_p, y_p) of perturbation, using the following expression (Jovanović and Popović, 2008b):

$$t_p [s] = \frac{r(x_p, y_p) [R_g]}{c [m \cdot s^{-1}]} = \frac{r_{x,y} \cdot GM_{BH}}{c^3}, \quad (23)$$

where $r_{x,y} = \frac{r(x_p, y_p)}{R_g}$, G is Newton's gravitational constant and M_{BH} is the mass of central black hole.

Using the time t_p [s] we are now able to obtain simulated light curves, produced as perturbation moves along the accretion disk. An example of such light curves, corresponding to displacement of perturbation along the receding side of the disk, is given in Fig. 14. From this figure it can be seen

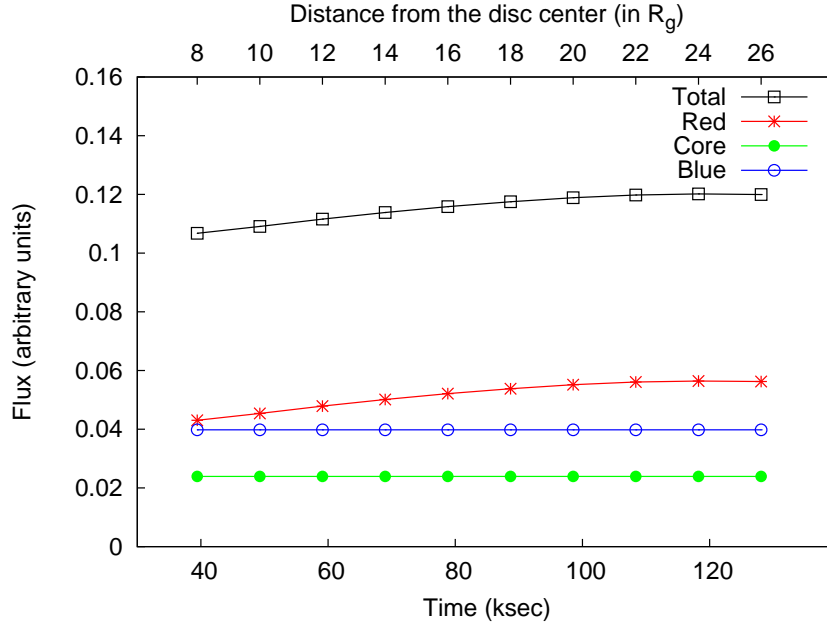


Figure 14: The simulated light curves in case of perturbing region displacement along the receding side of the disk and without rotation (Jovanović and Popović, 2008b). Light curves correspond to the following spectral bands: total flux (black) to 0.1 – 12.8 keV, ”red” to 0.1 – 6.1 keV, ”core” to 6.1 – 6.7 keV and ” blue” to 6.7 – 12.8 keV.

that displacement of perturbing region results in variations of only ”red” light curve (0.1 – 6.1 keV), while the ”blue” one (6.7 – 12.8 keV) and the line core (6.1 – 6.7 keV) stay nearly constant.⁶ These variations are then reflected in total line flux in 0.1 – 12.8 keV energy band (Jovanović and Popović, 2008b).

Thus, this perturbing model could explain the variable ”red” feature of the Fe $K\alpha$ line observed in NGC 3516. Besides, the realistic durations of disk emissivity perturbations are also obtained if a central supermassive black hole with mass $M_{BH} = 1 \times 10^9 M_{\odot}$ is assumed (Jovanović and Popović, 2008b).

⁶We should note here that we did not take into account the rotation which can produce periodical peaks in the light curves, as it can be seen from Fig. 12

6.2 Absorption by warm X-ray absorbers

The X-ray emission of AGN could be also significantly absorbed by an out-flowing wind, especially in case of so-called Low Ionization Broad Absorption Line (LoBAL) quasars. Recent observations of such quasars (e.g. Mrk 231 (Braitto et al., 2004) and H 1413+117 (Chartas et al., 2007)) confirmed the presence of X-ray absorbers in these objects. Wang et al. (2001) detected an absorption line at 5.8 keV in nearby ($z = 0.0033$) Seyfert 1.5 galaxy NGC 4151. A variable absorption line at the same energy has been discovered by Nandra et al. (1999) in NGC 3516 (Fig. 15) and was interpreted as a Fe K resonant absorption line, redshifted either by infalling absorbing material or by strong gravity in the vicinity of the black hole.

Done et al. (2007) found an evidence for a P Cygni profile of the Fe $K\alpha$ line (Fig. 16) in narrow line Seyfert 1 galaxies. According to these authors, complex X-ray spectra of these objects show strong "soft excess"

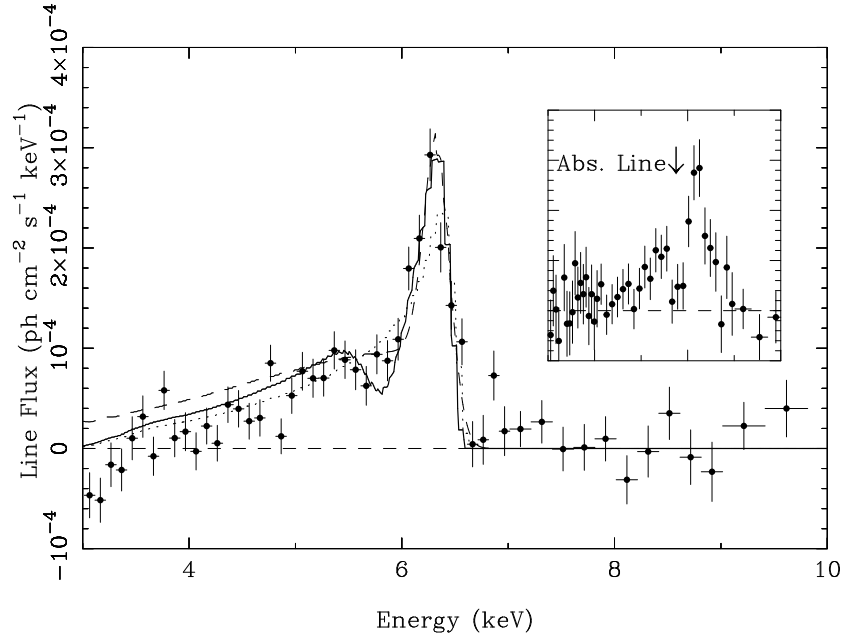


Figure 15: Absorption component at 5.8 keV in the red part of the Fe $K\alpha$ line of Seyfert 1 galaxy NGC 3516, observed by *ASCA* satellite (Nandra et al., 1999). The dashed line shows best fit with model of an accretion disk around a rotating (Kerr) black hole.

below 2 keV and a sharp drop at ~ 7 keV which can be explained either by reflection or by absorption from relativistic, partially ionized material close to the black hole. They showed that a sharp feature at ~ 7 keV results from absorption/scattering/emission of the iron $K\alpha$ line in the wind. In the case of 1H 0707-495 (Fig. 16), this absorption feature can be satisfactorily fitted by the P Cygni profile (Done et al., 2007).

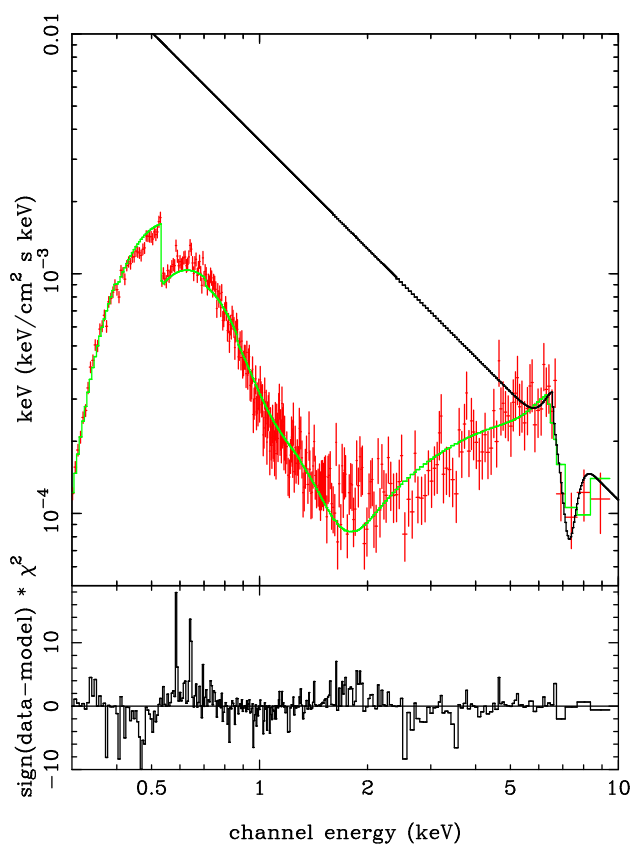


Figure 16: The full *XMM-Newton* spectrum of 1H 0707-495 with the best-fit model which involves a P Cygni profile for the iron features (Done et al., 2007). The lower panel shows residuals to the fit.

There are different models of the X-ray absorbing/obscuring regions, like absorbing medium comprised of cold absorbing cloudlets by Fuerst & Wu (2004), but here we will focus on the model given by Jovanović and Popović (2007), developed in order to study how much warm absorbers can change the Fe $K\alpha$ spectral line profile, emitted from a relativistic accretion disk. In

this model, absorption region is considered to be composed of a number of individual spherical absorbing clouds with the same small radii (see Fig. 17 left), scattered in space so that projections of their centers to the observer's sky plane (X_i, Y_i) have bivariate normal distribution $\mathcal{N}_2(\mu, \Sigma)$. Here, $\mu = [\mu_X, \mu_Y]^T$ and $\Sigma = \begin{bmatrix} \sigma_X^2 & \rho\sigma_X\sigma_Y \\ \rho\sigma_X\sigma_Y & \sigma_Y^2 \end{bmatrix}$, where μ_X and μ_Y are the means of X_i and Y_i , σ_X and σ_Y are their standard deviations and ρ is the correlation between them. Absorbing region presented in Fig. 17 (left) is obtained for the following parameters: $\rho = 0$, $\mu_X = X_A$, $\mu_Y = Y_A$ and $\sigma_X = \sigma_Y = R_A$, where (X_A, Y_A) is the center and R_A is the radius of projection of entire absorbing region.

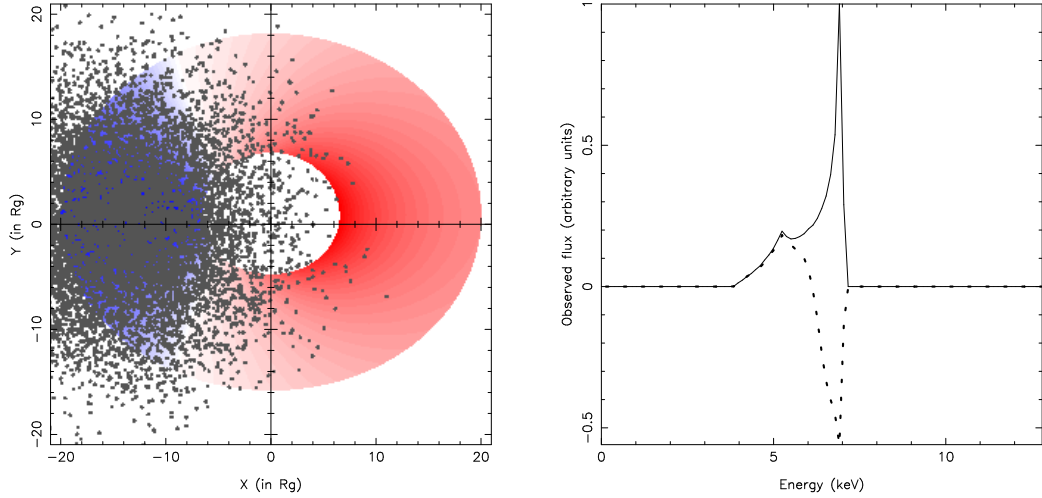


Figure 17: *Left*: Relativistic accretion disk in the Schwarzschild metric partially covered by a cloud of absorbing material (randomly scattered gray dots). *Right*: Comparison between the unabsorbed Fe K α spectral line profile (solid line) and corresponding absorbed profile (dotted line) caused by the absorbing/obscuring region presented in the left panel (Jovanović and Popović, 2007).

The absorption coefficient $A(X, Y)$ for every spherical cloud in the absorbing region is given by (Jovanović and Popović, 2007):

$$A(X, Y) = (1 - I_A(X, Y)) \cdot e^{-\left(\frac{g(X, Y) E_0 - E_A}{\sigma_E}\right)^2}, \quad (24)$$

where absorption intensity coefficient $I_A(X, Y)$ describes the distribution of absorption over the whole region, E_A is the central energy of absorption and σ_E is the width of absorption band (velocity dispersion).

A comparison between the unabsorbed Fe $K\alpha$ spectral line profile and the corresponding absorbed profile obtained by this absorption model is given in Fig. 17 (right). As it can be seen from Fig. 17, when the X-ray radiation from approaching side of the disk is significantly absorbed/obscured by the absorbing region, there is a very strong absorption of the iron line. In such case the emission Fe $K\alpha$ line looks redshifted at ~ 5 keV and is followed by a strong absorption line at ~ 7 keV (Fig. 17 right), which indicates the P Cygni profile of the iron line. Thus, this model can satisfactorily explain the P Cygni profile of the Fe $K\alpha$ line in the case when approaching side of the accretion disk is partially blocked from our view by the X-ray absorbing/obscuring material, while the rest of the disk is less absorbed/obscured and therefore is visible (Jovanović and Popović, 2007).

6.3 Gravitational microlensing

Some recent observational and theoretical studies suggest that gravitational microlensing can also induce variability in the X-ray emission of AGN, especially in the case of gravitationally lensed quasars. The phenomenology of gravitational lensing effects and introduction to this field has been given in several review papers and books. References to some of them can be found in e.g. Popović et al. (2002). Therefore, in this section we will not discuss all aspects of such effects in the universe, but instead, we will briefly present the basic concepts of gravitational microlensing theory, as well as some examples for microlensing influence on the X-ray emission from AGN.

Gravitational lensing is an universal natural phenomenon where the gravitational force of lensing object induce either the amplification of some background source (**microlensing**), or the appearance of its multiple images (**macrolensing**), due to light bending in a gravitational field of the deflector. Separation angle between the images of background source depends on the mass of gravitational lens and therefore, multiple images can be observed only in the case of a massive lensing object, such as galaxy. One of the most famous multiple image lens systems is quasar QSO 2237+0305, also known as Einstein Cross, which is located at redshift $z = 1.695$ (see Fig. 18). Its four images are due to lensing effect of galaxy ZW2237+030, located between us and the quasar at redshift $z = 0.0394$. In the case of a small mass

lens (e.g. a star), the separation angle is also small and therefore, different images of background source cannot be resolved. Instead, its intensity is amplified, causing the changes in the observed light curve. Common name for both, macrolensing (or simply lensing) and microlensing is **strong lensing**, contrary to **weak lensing**, which causes distortions in observed images of distant objects which can be then used for studying the mass distribution along the line of sight, but such phenomena will not be discussed here.

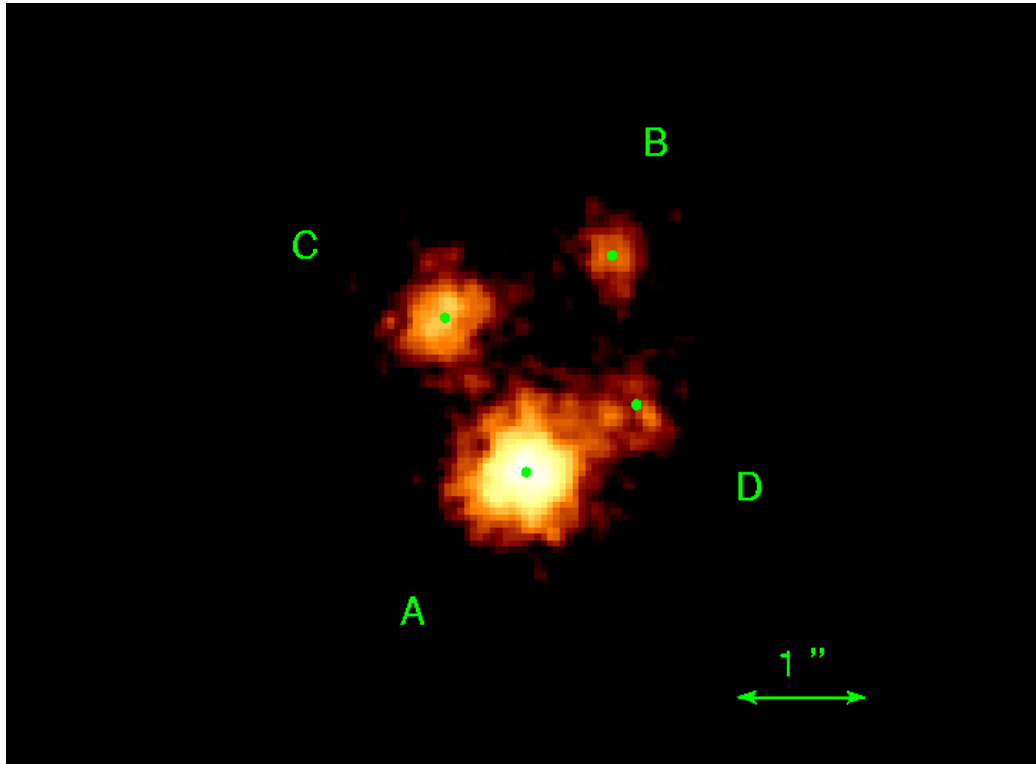


Figure 18: Gravitationally lensed system QSO 2237+0305 (Einstein Cross) observed by the *Advanced CCD Imaging Spectrometer (ACIS)* onboard the *Chandra X-ray Observatory* (Dai et al., 2003). The green circles in each image are the corresponding *Hubble Space Telescope (HST)* image positions provided by *CASTLES* (<http://cfawww.harvard.edu/glensdata/Individual/Q2237.html>).

Zakharov et al. (2004) found that cosmologically distributed microlenses could significantly contribute to the X-ray variability of high-redshifted ($z >$

2) QSOs. Indeed, microlensing of the Fe K α line has been reported at least in three macrolensed QSOs: MG J0414+0534 (Chartas et al., 2002), QSO 2237+0305 (Dai et al., 2003), and H 1413+117 (Oshima et al., 2001; Chartas et al., 2004). Chartas et al. (2002) detected an increase of the Fe K α equivalent width in the image B of MG J0414+0534 which was not followed by the continuum and explained this behavior by assumption that the thermal emission region of the disk and the Compton up-scattered emission region of the hard X-ray source lie within smaller radii than the iron-line reprocessing region. Analyzing the X-ray variability of QSO 2237+0305A, Dai et al. (2003) also measured amplification of the Fe K α line in component A of QSO 2237+0305 but not in the continuum and suggested that the larger size of the continuum emission region in comparison to the Fe K α emission region could explain this result. In the case of H 1413+117, Chartas et al. (2004) found that the continuum and the Fe K α line were enhanced by a different factor. For more detailed discussion about observational and theoretical investigations of the X-ray variability in gravitationally lensed QSOs see e.g. Jovanović et al. (2003); Jovanović (2005); Jovanović & Popović (2005); Jovanović (2006); Jovanović et al. (2008) and Popović et al. (2006a), and also references therein.

The influence of gravitational microlensing on the X-ray emission from a compact accretion disk of AGN can be studied using numerical simulations based on ray-tracing method described in §5.3 of this chapter. In the following text we will briefly review three models of gravitational microlenses (point-like, straight-fold caustic and quadruple microlens), as well as their influence on the X-ray radiation of AGN.

If X and Y are the impact parameters (i.e. the coordinates) which describe the apparent position of each point of the accretion disk image on the celestial sphere as seen by an observer at infinity, then the amplified brightness (due to gravitational microlensing influence) is given by (Jovanović et al., 2003; Popović et al., 2003a,b):

$$I_p(X, Y) = \varepsilon(X, Y)g^4(X, Y)\delta(x - g(X, Y))A(X, Y), \quad (25)$$

where $x = \nu_{obs}/\nu_0$ (ν_0 and ν_{obs} are the transition and observed frequencies, respectively), $g = \nu_{obs}/\nu_{em}$ is the shift due to relativistic effects (ν_{em} is the emitted frequency), ε is the disk emissivity and A is the amplification caused by microlensing. Usually, we do not know the exact form of A , so we are forced to consider the different approximations in order to estimate this quantity.

The first of these approximations is called **point-like microlens**, and it is applied when an isolated compact object (e.g. a star) plays a role of gravitational microlens. Such microlens is characterized by its Einstein Ring Radius in the lens plane (Jovanović et al., 2008):

$$ERR = \sqrt{\frac{4Gm}{c^2} \frac{D_l D_{ls}}{D_s}} \quad (26)$$

or by the corresponding projection to the source plane:

$$\eta_0 = \frac{D_s}{D_l} ERR = \sqrt{\frac{4Gm}{c^2} \frac{D_s D_{ls}}{D_l}}, \quad (27)$$

where G is the gravitational constant, c is the speed of light, m is the microlens mass and D_l , D_s and D_{ls} are the cosmological angular distances between observer-lens, observer-source and lens-source, respectively. In this case, the amplification is given by the following relation (Narayan & Bartelmann, 1999; Popović et al., 2001; Jovanović et al., 2003):

$$A(X, Y) = \frac{u^2(X, Y) + 2}{u(X, Y) \sqrt{u^2(X, Y) + 4}}, \quad (28)$$

where

$$u(X, Y) = \frac{\sqrt{(X - X_0)^2 + (Y - Y_0)^2}}{\eta_0} \quad (29)$$

corresponds to the angular separation between the microlens and a source. X_0, Y_0 are the coordinates of the microlens with respect to the disk center (given in R_g).

The total observed flux is then given by (Jovanović et al., 2003; Popović et al., 2003a,b):

$$F(x) = \int_{image} I_p(x) d\Omega \quad (30)$$

where $d\Omega$ is the solid angle subtended by the disk in the observer's sky and the integral extends over the whole disk image.

An illustration of a point-like gravitational microlens crossing over an accretion disk in the Kerr metric with angular momentum $a = 0.998$ is presented in Fig. 19 (Popović et al., 2002, 2003b). The simulated unamplified and amplified Fe $K\alpha$ line profiles due to different positions of the microlens are shown in Fig. 20 (Popović et al., 2003a).

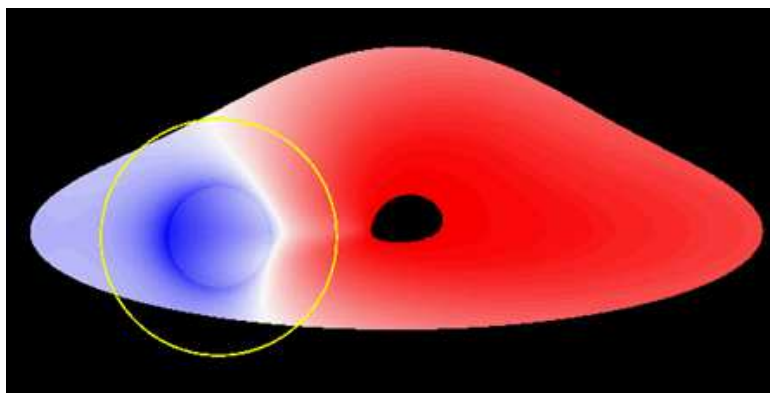


Figure 19: Illustration of a point-like gravitational microlens crossing over an accretion disk in Kerr metric with angular momentum $a = 0.998$ (Popović et al., 2002, 2003b). Einstein Ring of the microlens is schematically presented by yellow Euclidian circle.

From Fig. 20 it can be seen that point-like microlens could induce strong changes of the Fe $K\alpha$ line shape and intensity, depending on the location of the microlens. In the first place, we have in mind the changes in number of peaks, their relative separation and the peak velocity. Secondly, such transit of the point-like microlens could cause an asymmetrical enhancement of the line profile, and the maximum of the amplification would be obtained for negative values of x -coordinate, i.e. for the approaching side of the rotating accretion disk, and therefore it would affect mainly the blue part of the Fe $K\alpha$ line.

In most cases we cannot simply consider that microlensing is caused by an isolated compact object, but we should take into account that such micro-deflector is located in an extended object (typically, the lens galaxy). Therefore, when the size of the microlens projected Einstein Ring Radius is larger than the size of the accretion disk and when a number of microlenses form a caustic net, we describe the microlensing effects by a **straight-fold caustic** approximation (Jovanović et al., 2008; Popović et al., 2003a), where the amplification at a point of an extended source (accretion disk) close to the caustic is given by (Chang & Refsdal, 1984):

$$A(X, Y) = A_0 + K \sqrt{\frac{r_{caustic}}{\kappa(\xi - \xi_c)}} \cdot H(\kappa(\xi - \xi_c)). \quad (31)$$

In above expression A_0 is the amplification outside the caustic and $K = A_0\beta$

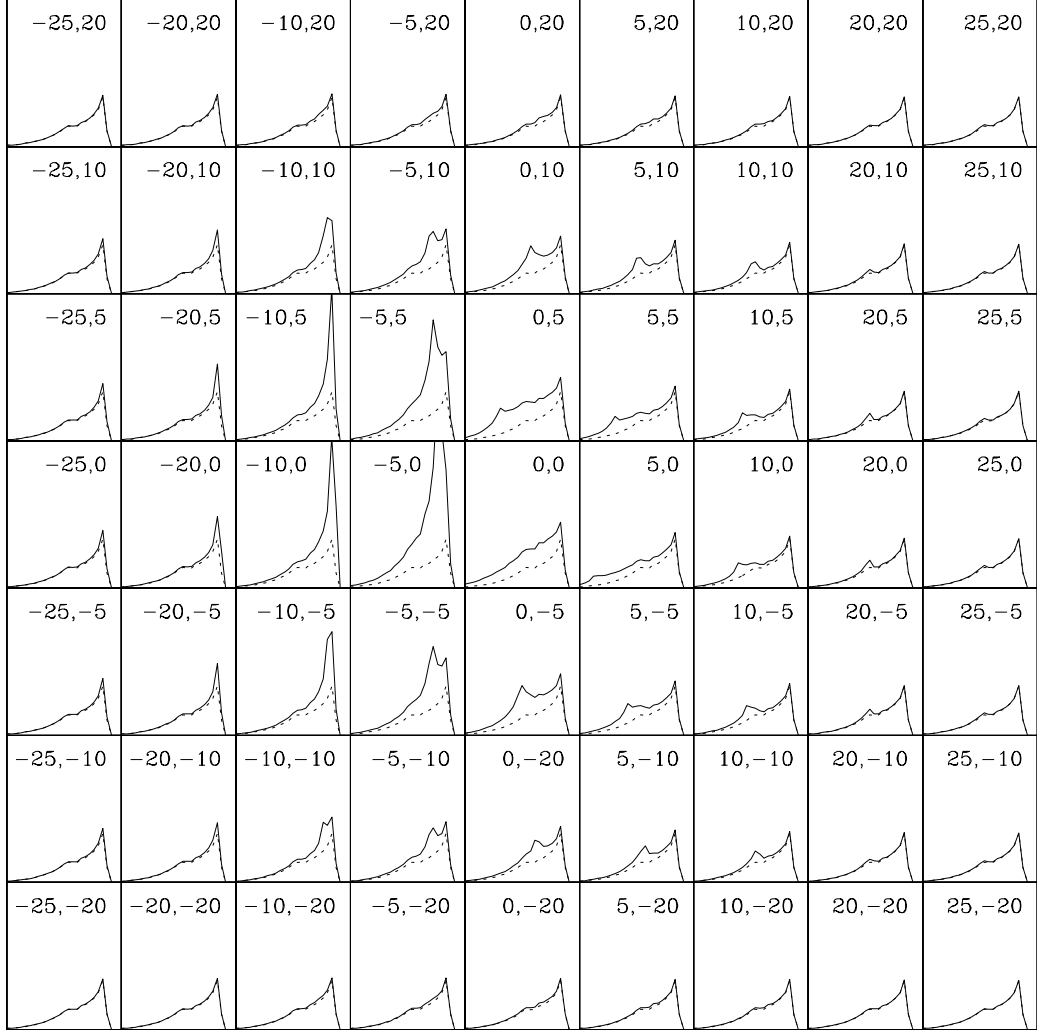


Figure 20: The unamplified (dotted line) and amplified Fe K α line profiles (solid line) for different positions of the point-like microlens, which coordinates (expressed in R_g) in respect to the accretion disk center are given at the top of each panel (Popović et al., 2003a). The simulations are performed for an accretion disk in Kerr metric with angular momentum $a = 0.998$ and with the following disk parameters: $R_{in} = 6 R_g$, $R_{out} = 20 R_g$, $i = 35^\circ$, $q=2.5$. The Einstein Ring Radius of the point-like microlens is $10 R_g$. The relative intensity (y -axis) is in the range from 0 to 3, and energy shift g due to relativistic effects (x -axis) is in the range from 0.4 to 1.2.

is the caustic amplification factor, where β is constant of order of unity. ξ is the distance perpendicular to the caustic and ξ_c is the minimum distance from the disk center to the caustic (both in R_g). The "caustic size" $r_{caustic}$ is the distance ξ for which the caustic amplification is equal to 1, and therefore this parameter defines a typical linear scale for the caustic. $H(\kappa(\xi - \xi_c))$ is the Heaviside function which equals 1 for $\kappa(\xi - \xi_c) > 0$ and otherwise it is 0. κ is ± 1 depending on the direction of caustic motion: if the direction of the caustic motion is from approaching side of the disk $\kappa = -1$, otherwise it is $+1$. Also, in the special case of caustic crossing perpendicular to the rotating axis $\kappa = +1$ for direction of caustic motion from $-Y$ to $+Y$, otherwise it is -1 .

A microlensing event where a caustic crosses over an accretion disk can be described in the following way (Jovanović et al., 2008): before the caustic reaches the disk, the amplification is equal to A_0 because the Heaviside function of Eq. (31) is zero. Just as the caustic begins to cross the disk, the amplification rises rapidly and then decays gradually towards A_0 as the source moves away from the caustic-fold.

An illustration of the straight-fold caustic crossing over an accretion disk in Schwarzschild metric is presented in Fig. 21, and the corresponding effects on the shapes of the X-ray continuum and the Fe $K\alpha$ line are shown in Fig. 22 (Jovanović, 2006; Popović et al., 2003b). As it can be seen from Fig. 22, caustics could also induce significant amplifications of both, the X-ray continuum and Fe $K\alpha$ line.

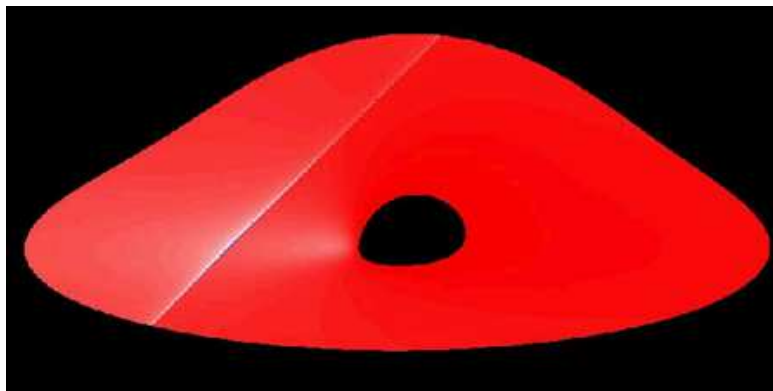


Figure 21: Illustration of a straight-fold caustic gravitational microlens crossing over an accretion disk in Schwarzschild metric (Jovanović, 2006; Popović et al., 2003b).

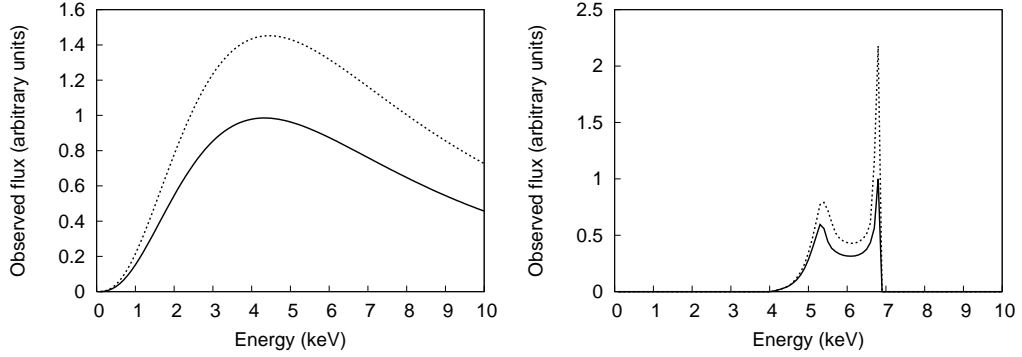


Figure 22: The deformations of the X-ray continuum (left) and the Fe $K\alpha$ line (right) due to influence of straight-fold caustic from Fig. 21. Undeformed profiles are presented by solid and deformed by dotted lines (Jovanović, 2006).

The most complex approximation for gravitational microlensing amplification is so called **quadruple microlens**. This model is applied to obtain a spatial distribution of magnifications in the source plane (where an accretion disk of AGN is located), produced by a random star field placed in the lens plane. Such spatial distribution of magnifications is called **microlensing map, microlensing pattern or caustic network**. If we consider a set of N compact objects (e.g. stars) which are characterized by their positions x_i and their masses m_i , then the normalized lens equation is given by (Abajas et al., 2007):

$$\vec{y} = \sum_{i=1}^N m_i \frac{\vec{x} - \vec{x}_i}{|\vec{x} - \vec{x}_i|^2} + \begin{bmatrix} 1 - \kappa_c + \gamma & 0 \\ 0 & 1 - \kappa_c - \gamma \end{bmatrix} \vec{x}, \quad (32)$$

where \vec{x} and \vec{y} are the normalized image and source positions, respectively. The sum describes the light deflection by the stars and the last term is a quadruple contribution from the galaxy containing the stars, where κ_c is a smooth surface mass density and γ is an external shear. The total surface mass density or convergence can be written as $\kappa = \kappa_* + \kappa_c$, where κ_* represents the contribution from the compact microlenses. The corresponding microlensing map is then defined by two parameters: the convergence - κ , and the shear due to the external mass - γ .

For some specific lensing event one can model the corresponding magnification map using numerical simulations based on ray-shooting techniques (see

e.g. Jovanović et al. (2008); Popović et al. (2006a,b) and references therein), in which the rays are shot from the observer to the source, through the randomly generated star field in the lens plane. An example of a magnification map for a "typical" lens system (i.e. for a lens system where the redshifts of microlens and source are $z_l = 0.5$ and $z_s = 2$, respectively) is presented in the left panel of Fig. 23, and the corresponding X-ray, UV and optical continuum variations are given in the right panel of the same figure (Jovanović et al., 2008). The size of this magnification map is $16 \eta_0 \times 16 \eta_0$ and it is generated using the following arbitrary values for convergence and shear: $\kappa = 0.45$ and $\gamma = 0.3$. The light curves in the right panel of Fig. 23 are produced when an accretion disk crosses over the magnification pattern in the left panel, along the path denoted by the white solid line.

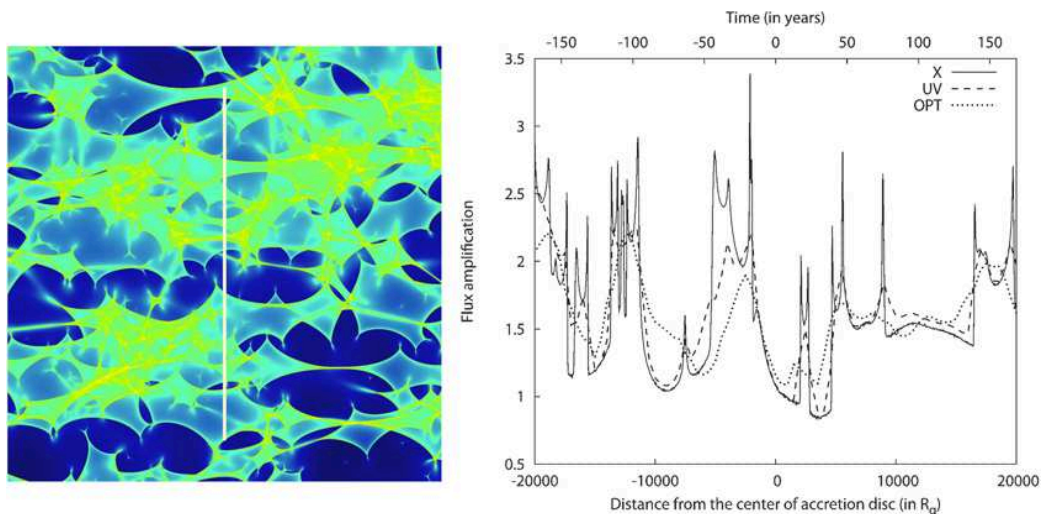


Figure 23: *Left:* Magnification map of a "typical" lens system, where the white solid line represents a path of an accretion disk center. *Right:* Variations in the X-ray (solid), UV (dashed) and optical (dotted) spectral bands corresponding to the path in the magnification map of a "typical" lens system (left).

As one can see from Fig. 23 (right), the variations of the X-ray continuum due to microlensing are much stronger and faster in comparison to the variations in UV and optical spectral bands (Jovanović et al., 2008; Popović et al., 2006a,b). Usually, so called High Amplification Events, i.e. asymmetric peaks in the light curves are also analyzed (Jovanović et al., 2008). The re-

sults presented in Fig. 23 (right) show that the rise times of such events are the shortest and their frequency the highest in the X-rays, in comparison to the UV/optical spectral bands.

In order to explain the observed X-ray variability in gravitationally lensed quasars, Popović et al. (2006a) considered a microlensing magnification map for a specific case of the QSO 2237+0305A image (Fig. 24, top). This map with $1 \eta_0 \times 2 \eta_0$ on a side was generated using the following parameters: $\kappa = 0.36$, $\gamma = 0.40$ and the mean mass of randomly distributed deflectors $\langle m \rangle = 0.35 M_\odot$. The corresponding variations of the total Fe K α line and X-ray continuum fluxes are presented in Fig. 24 (bottom).

As one can see from Fig. 24 (bottom), there is a global correlation between the total line and continuum fluxes during the complete simulated microlensing event, but while the continuum flux variations are smooth and slow, the line flux varies much stronger and faster (Jovanović, 2005). Moreover, there is a certain period in the middle of the microlensing event in which the Fe K α line flux changes rapidly, while the continuum flux remains nearly constant. This indicates that different behavior of the line and X-ray continuum variability, observed in some lensed quasars (Chartas et al., 2002, 2004), may be explained by microlensing hypothesis if the line originates from the innermost part of the accretion disk, while the X-ray continuum is emitted from a larger region in the disk (Jovanović et al., 2003; Jovanović, 2005; Jovanović & Popović, 2005; Popović et al., 2006a).

On the basis of all facts presented in this section, one can conclude that gravitational microlensing can produce significant variations and amplifications of the Fe K α line and X-ray continuum. During a microlensing event, even very small mass objects could produce noticeable changes in the X-ray radiation from accretion disks of AGN. These changes are significantly larger than the corresponding effects in the optical and UV emission. Also, microlensing hypothesis can satisfactorily explain the excess in the iron line emission, observed in some gravitational lens systems.

7 Conclusion

In this chapter we discussed the X-ray radiation from relativistic accretion disks around supermassive black holes, supposed to exist in the centers of all Active Galactic Nuclei. The X-ray radiation is created when the accreting material loses its angular momentum due to friction between the adjacent

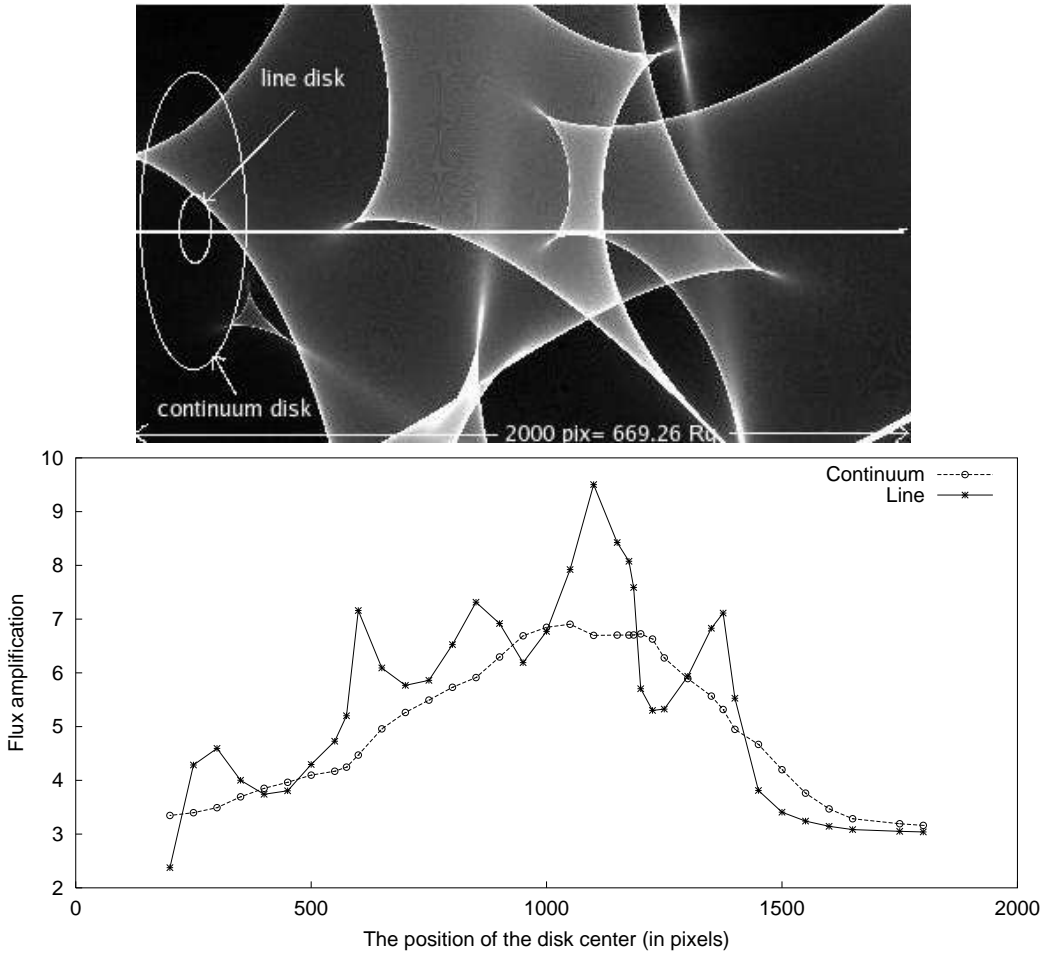


Figure 24: *Top*: Microlensing magnification map of QSO 2237+0305A image with $1 \eta_0 \times 2 \eta_0$ on a side and a scheme of an accretion disk with separated Fe $K\alpha$ line and X-ray continuum emitting regions which outer radii are 20 and 100 R_g , respectively (Popović et al., 2006a). The straight horizontal line represents a path of the disk center. *Bottom*: The corresponding amplifications of the Fe $K\alpha$ line and X-ray continuum total fluxes for different positions of the disk center along the path on the magnification map in the left panel.

layers in the disk and spiral towards the central black hole, releasing the gravitational energy. Part of this energy increases the kinetic energy of rotation and the rest is turned into the radiation, which is then emitted from the disk surface in the X-ray, UV and optical spectral bands. It is the only known

mechanism of converting gravitational potential energy into radiation, which is sufficiently efficient to explain the high luminosities of some observed AGN.

The standard model of an accretion disk, including its emission, accretion rate, luminosity, structure and spectral distribution was described in details. A significant part of this chapter was devoted to modeling of the observed X-ray radiation in both the Fe $K\alpha$ spectral line and X-ray continuum. The modeled X-ray radiation is then used to analyze the several effects of strong gravity in the vicinity of black holes which have the influence on the shapes and intensities of the observed Fe $K\alpha$ line and X-ray continuum. We showed that the X-ray emission strongly depends on the angular momentum and mass of the central black hole, as well as on several parameters describing the X-ray emitting region in the disk. This was demonstrated on several examples, showing various aspects of the X-ray emission from the accretion disk around Schwarzschild and Kerr black holes. Since the X-ray radiation is probably produced in a very compact region near the black holes, such comparison between observed and modeled X-ray radiation can provide us some essential information about the plasma conditions and the space-time geometry in the vicinity of those black holes.

We also studied some possible causes for the rapid and irregular variability of the Fe $K\alpha$ line and X-ray continuum, observed in the X-ray spectra of some AGN. Our results show that, at least, three mechanisms could explain such variability: perturbations of disk emissivity, absorption by warm X-ray absorbers and gravitational microlensing.

Taking all this into account, we can conclude that the X-ray emission from accretion disks of AGN can be used as a powerful tool for revealing the physics and geometry in the vicinity of their central supermassive black holes. But, to use the Fe $K\alpha$ line profile for such investigations, one should also take into account the effects which can disturb its profile (such as e.g. absorption, perturbations in the disk and gravitational lensing).

Acknowledgements. This work is a part of the project (146002) "Astrophysical Spectroscopy of Extragalactic Objects" supported by the Ministry of Science of Serbia.

References

- Abajas, C., Mediavilla, E., Muñoz, J. A., Gómez-Álvarez, P., Gil-Merino, R. *ApJ*, 2007, *658*, 748
- Antonucci, R. *ARA&A*, 1993, *31*, 473
- Antonucci, R., Barvainis, R. *ApJ*, 1988, *332L*, 13
- Antonucci, R. R. J., Miller, J. S. *ApJ*, 1985, *297*, 621
- Armitage, P. J., Reynolds, C. S. *MNRAS*, 2003, *341*, 1041
- Ballantyne D. R., Fabian, A.C. *ApJ*, 2005, *622*, L97
- Bao, G., Hadrava, P., Ostgaard, E. *ApJ*, 1994, *435*, 55
- Bianchi, S., La Franca, F., Matt, G. et al. *MNRAS*, 2008, *389L*, 52B
- Binney, J., Merrifield, M. *Galactic astronomy*, Princeton University Press: Princeton, New Jersey, 1998
- Bon, E., Popović, L. Č., Ilić, D., Mediavilla, E. G. *New. Ast. Rev.*, 2006, *50*, 716.
- Braitto, V., Della Ceca, R., Piconcelli, E., Severgnini, P., Bassani, L., Cappi, M., Franceschini, A., Iwasawa, K., Malaguti, G., Marziani, P., Palumbo, G. G. C., Persic, M., Risaliti, G., Salvati, M. *A&A*, 2004, *420*, 79
- Brandt, W. N., Hasinger, G. *ARA&A*, 2005, *43*, 827
- Brenneman, L. W., Reynolds, C. S. *ApJ*, 2006, *652*, 1028
- Bromley, B.C., Chen, K., Miller, W.A. *ApJ*, 1997, *475*, 57
- Čadež, A., Fanton, C., Calivani, M. *New Astronomy*, 1998, *3*, 647
- Carter, B. *Black Holes*, Eds. De Witt, C. and De Witt, B. S., Gordon and Breach: New York, 1973
- Chandrasekhar, S. *The Mathematical Theory of Black Holes*, Oxford University Press: New York, 1983
- Chang, K., Refsdal, S. *A&A*, 1984, *132*, 168

- Chartas, G., Agol, E., Eracleous, M., Garmire, G., Bautz, M. W., Morgan, N. D. *ApJ*, 2002, *568*, 509
- Chartas, G., Eracleous, M., Agol, E., Gallagher, S. C. *ApJ*, 2004, *606*, 78
- Chartas, G., Eracleous, M., Dai, X., Agol, E., Gallagher, S. *ApJ*, 2007, *661*, 678
- Clavel, J., Schulz, B., Altieri, B., Barr, P., Claes, P., Heras, A., Leech, K., Metcalfe, L., Salama, A. *A&A*, 2000, *357*, 839
- Corral, A., Page, M.J., Carrera, F.J., Barcons, X. Mateos, S., Ebrero, J., Krumpe, M., Schwope, A., Tedds, J.A., Watson, M.G. *A&A*, 2008, *492*, 71
- Dabrowski, Y., Fabian, A. C., Iwasawa, K., Lasenby, A. N., Reynolds, C. S., *MNRAS*, 1997, *288*, L11
- Dai, X., Chartas, G., Agol, E., Bautz, M. W., Garmire, G.P. *ApJ*, 2003, *589*, 100
- Done, C., Sobolewska, M. A., Gierliński, M., Schurch, N. J. *MNRAS*, 2007, *374*, L15
- Dovčiak, M., Karas, V., Yaqoob, T. *ApJ*, 2004, *153*, 205
- Eracleous, M., Halpern, J. P. *ApJS*, 1994, *90*, 30
- Eracleous, M., Halpern, J. P. *ApJS*, 2003, *599*, 886
- Fabian, A. C. *ESASP*, 2006, *604*, 463
- Fabian A.C., Vaughan S., *MNRAS*, 2003, *340*, 28
- Fabian, A. C., Rees, M. J., Stella, L. & White, N. E. *MNRAS*, 1989, *238*, 729
- Fabian, A. C., Iwasawa, K., Reynolds, C. S., Young, A. J. *PASP*, 2000, *112*, 1145
- Fanton, C., Calivani, M., Felice, F., Čadež, A. *PASJ*, 1997, *49*, 159
- Ferland, G. J., Korista, K. T., Peterson, B. M. *ApJ*, 1990, *363L*, 21

- Ferrarese, L., Ford, H. *SSRv*, 2005, *116*, 523
- Flohic, H. M. L. G., Eracleous, M. *ApJ*, 2008, *686*, 138
- Fuerst, S. V., Wu, K. *A&A*, 2004, *424*, 733
- Harris, D. E., Krawczynski, H. *ARA&A*, 2006, *44*, 463
- Hawking, S. *A Brief History of Time*, Bantam Books: New York, 1988
- Hubble, E. *ApJ*, 1926, *54*, 368
- Ilić, D., Popovć, L. Č., Bon, E. Mediavilla, E. G., Chavushyan, V. H. *MNRAS*, 2006, *371*, 1610
- Iwasawa, K., Miniutti, G., Fabian, A.C. *MNRAS*, 2004, *355*, 1073
- Jovanović, P., Popović, L. Č., Dimitrijević, M. S. *PAOB*, 2003, *76*, 205
- Jovanović, P. *Mem. SAI*, 2005, *7*, 56
- Jovanović, P., Popović, L. Č. *PASRB*, 2005, *5*, 195
- Jovanović, P. *PASP*, 2006, *118*, 656
- Jovanović, P., Popović, L. Č. *AIP Conf. Proc.*, 2007, *938*, 76
- Jovanović, P., Zakharov, A.F., Popović, L.Č., Petrović, T. *MNRAS*, 2008, *386*, 397
- Jovanović, P., Popović, L. Č. *Fortschr. Phys.*, 2008a, *56*, No. 4 – 5, 456
- Jovanović, P., Popović, L. Č. *PAOB*, 2008b, *84*, 467
- Kaspi, S., Smith, P. S., Netzer, H., Maoz, D., Jannuzi, B. T., Giveon, U. *ApJ*, 2000, *533*, 631
- Khachikian, E. Y., Weedman, D. W. *ApJ*, 1974, *192*, 581
- Krolik, J. H. *Active Galactic Nuclei*, Princeton University Press: Princeton, New Jersey, 1999
- Laor A., *ApJ*, 1991, *376*, 90

- Li, L., Zimmerman, E. R., Narayan, R., McClintock, J. E. *ApJS*, 2005, *157*, 335
- Malzac, J. *Mem. S.A.It.*, 2007, *78*, 382
- Markowitz, A., Reeves, J. N., Miniutti, G., et al. *PASJ*, 2008, *60S*, 277
- Miller, J. M. *ARA&A*, 2007, *45*, 441
- Nandra, K., George, I.M., Mushotzky, R.F., Turner, T.J. & Yaqoob, T. *ApJ*, 1997, *477*, 602
- Nandra, K., George, I. M., Mushotzky, R. F., Turner, T. J., Yaqoob, T. *ApJ*, 1999, *523*, 17
- Nandra K., O'Neill P.M., George I.M., Reeves N., *MNRAS*, 2007, *382*, 194
- Narayan, R., Bartelmann, M. *in Formation of Structure in the Universe*, Eds. Dekler, A., Ostriker, J.P., Cambridge University Press, 1999, p. 360
- Oke, J. B., Sargent, W. L. W. *ApJ*, 1968, *151*, 807
- Oshima, T., Mitsuda, K., Fujimoto R., Iyomoto N., Futamoto K., et al. *ApJ*, 2001, *563*, L103
- Osterbrock, D. E. *Astrophysics of Gaseous Nebulae and Active Galactic Nuclei*, University Science Book, 1989
- Peterson, B. M. *An Introduction to Active Galactic Nuclei*, Cambridge University Press, 2004
- Peterson, B. M., Ferrarese, L., Gilbert, K. M., et al. *ApJ*, 2004, *613*, 682
- Peterson, B. M., Wandel, A. *ApJ*, 2000, *540L*, 13
- Popović, L., Č., Mediavilla, E.G., Muñoz J., Dimitrijević, M.S., Jovanović, P. *SerAJ*, 2001, *164*, 73
- Popović, L.Č., Jovanović, P., Bon, E., Dimitrijević, M.S. *PAOB*, 2002, *73*, 49
- Popović, L.Č., Mediavilla, E.G., Jovanović, P., Muñoz, J.A. *A&A*, 2003a, *398*, 975

- Popović, L.Č., Jovanović, P., Mediavilla, E.G., Muñoz, J.A. *Astron. Astrophys. Transactions*, 2003b, *22*, 719
- Popović, L. Č., Mediavilla, E. G., Bon, E., Ilić, D., *A&A*, 2004, *423*, 909
- Popović, L. Č., Jovanović, P., Mediavilla, E.G., Zakharov, A.F., Abajas, C., Muñoz, J.A., Chartas, G. *ApJ*, 2006a, *637*, 620
- Popović, L.Č., Jovanović, P., Petrović, T., Shalyapin, V. N. *AN*, 2006b, *10*, 981
- Popović, L. Č., Bon, E., Gavrilović, N. *Rev. Mex. A&A Conf.*, 2008, *32*, 99
- Reynolds, C. S., Fabian, A. C. *ApJ*, 2008, *675*, 1048
- Reynolds C. S, Nowak M. A., *Phys.Rep.*, 2003, *377*, 389
- Risaliti, G., Maiolino, R., Salvati, M. *ApJ*, 1999, *522*, 157
- Schwarzschild, K. *Sitzungsberichte der Deutschen Akademie der Wissenschaften zu Berlin, Klasse für Mathematik, Physik, und Technik*, 1916a, 189
- Schwarzschild, K. *Sitzungsberichte der Deutschen Akademie der Wissenschaften zu Berlin, Klasse für Mathematik, Physik, und Technik*, 1916b, 424
- Seyfert, C. K. *ApJ*, 1943, *97*, 28
- Schneider, P. *Extragalactic Astronomy and Cosmology An Introduction*, Springer-Verlag GmbH: Heidelberg, 2006
- Shakura, N.I., & Sunyaev, R.A. *A&A*, 1973, *24*, 337
- Shapovalova, A. I, Popović, L. Č., Collin, S., et al. *A&A*, 2008, *486*, 99
- Shields, G.A. *Nature*, 1978, *272*, 706
- Sunyaev, R. A., Titarchuk, L. G. *A&A*, 1980, *86*, 121
- Tanaka, Y., Nandra, K., Fabian, A. C., Inoue, H., Otani, C., Dotani, T., Hayashida, K., Iwasawa, K., Kii, T., Kunieda, H., Makino, F., Matsuoka, M. *Nature*, 1995, *375*, 659

- Turner, T. J., George, I. M., Nandra, K., Mushotzky, R. F. *ApJ*, 1997, *488*, 164
- Ulrich, M. H., Boksenberg, A., Bromage, G., et al. *MNRAS*, 1980, *192*, 561
- Wang, J., Wang, T., Zhou, Y. *ApJ*, 2001, *549*, 891
- Yaqoob, T., Reeves, J. N., Markowitz, A., Serlemitsos, P. J., Padmanabhan, U. *ApJ*, 2005, *627*, 156
- Zakharov, A. F., Popović, L. Č., Jovanović, P. *A&A*, 2004, *420*, 881
- Zhou, Y. Y., Yu, K. N., Young, E. C. M., Wang, J. M., Ma, E. *ApJ*, 1997, *475L*, 9
- Życki, P. T. *MNRAS*, 2004, *351*, 1180